Journal of Sound and Vibration 642 (2026) 119952

Contents lists available at ScienceDirect

Journal of Sound and Vibration

journal homepage: www.elsevier.com/locate/jsvi

Self-sustained whistling in long-cavity Helmholtz resonators with bias flow: Experimental characterization and analytical modelling

Andrey R. da Silva [a,*], Niklaus Lima [a], Julio Cordioli [a], Tsukasa Yoshinaga [b], Tercio L. Pereira [c]

[a] Department of Mechanical Engineering, Federal University of Santa Catarina, Campus Trindade, Florianópolis, 88036-000, Santa Catarina, Brazil
[b] Department of Mechanical Sciences and Bioengineering, Osaka University, Toyonaka, 00001, Osaka, Japan
[c] Faculty of Aerospace Engineering, Delft University of Technology, Kluyverweg 1, Delft, 2629HS, The Netherlands

ARTICLE INFO

Keywords:
Double-neck Helmholtz resonator
Shear layer instability
Self-sustained oscillation

ABSTRACT

This study examines the hydrodynamic-acoustic feedback mechanisms responsible for whistling in double-neck Helmholtz resonators under bias flow, with emphasis on long-cavity configurations representative of human whistling. Combined flow and acoustic experiments were performed using particle image velocimetry and pressure measurements to characterize vortex dynamics, sound generation, and oscillation regimes across a range of Reynolds numbers and geometric parameters. Within the self-sustained oscillation regime, sound pressure levels scale consistently with the Strouhal number, exhibiting a peak near $St = 0.32$. Experimental data collapse is achieved using a modified Reynolds number that incorporates cavity-length effects. Moreover, two-point coherence and cross-spectral analyses show that acoustic generation occurs predominantly inside the resonator chamber, with maximum sound production located approximately 2.3 diameters downstream of the upstream neck. Flow visualization reveals that vortices dissipate before reaching the downstream neck, indicating a feedback mechanism distinct from classical hole-tone and Rossiter-type oscillations. To interpret these findings, an empirical model was developed, consisting of a two-degree-of-freedom lumped acoustic system coupled to a nonlinear oscillator representing vortex shedding. The model reproduces the onset, lock-in, saturation, and abrupt extinction of self-sustained oscillations, capturing the essential coupling that transfers energy from the mean flow to the acoustic field. These results provide new insight into long-cavity whistles and offer a predictive framework for Helmholtz-type resonators under bias flow.

1. Introduction

Aerodynamic whistling is a compelling phenomenon that normally emerges from the coupling between shear layer instabilities and acoustic fields. From an engineering standpoint, whistling is generally regarded as an undesirable byproduct, as it is associated with intense pressure fluctuations in a wide range of systems, including corrugated pipes for mass transportation [1,2], combustion chambers [3,4], wind-tunnel test sections [5,6], and buffeting noise of ground vehicles [7,8]. In such contexts, aerodynamic whistling is frequently implicated in elevated noise levels, reductions in operational efficiency, and, in severe cases, structural fatigue [9,10].

Apart from its dramatic consequences, whistling also serves as an important means of human communication, functioning as a surrogate for spoken language in contexts where an enhanced signal-to-noise ratio is advantageous. By concentrating acoustic energy

* Corresponding author.
E-mail address: andrey.dasilva@lva.ufsc.br (A.R. da Silva).

https://doi.org/10.1016/j.jsv.2026.119952
Received 5 March 2026; Received in revised form 4 June 2026; Accepted 8 June 2026
Available online 10 June 2026

into narrow frequency bands, it facilitates long-distance communication and improves intelligibility under adverse environmental conditions [11,12]. Furthermore, whistling holds cultural significance, appearing in musical traditions, contests, and professional performances across diverse regions of the world.

Sondhauss [13] was the first to carry out a formal parametric study of a form of whistling known as the hole tone. This phenomenon occurs when two plates, each with an orifice of roughly the same diameter, are placed a short distance apart. Airflow injected through the first (upstream) orifice forms a jet, which, under certain flow conditions, produces a single-frequency tone as it passes through the second orifice. In his study, a wide variety of jet-edge configurations was considered, including different orifice sizes, shapes, edge sharpnesses, and plate spacings. Although results were primarily qualitative, it was observed that whistling frequency was proportional to the square root of the driving pressure and inversely proportional to the distance between orifices.

Almost two decades later, Rayleigh proposed the concept of a feedback loop to explain the self-sustained oscillations in whistling, or bird calls, produced by the "unaided mouth" [14]. In Rayleigh's hypothesis, instabilities in the jet formed in the upstream orifice propagate downstream until they interact with the second orifice. This interaction generates pressure fluctuations that travel upstream at the speed of sound, reinforcing the initial jet instability at the upstream constriction and sustaining the oscillatory process. Rayleigh further proposed that the oscillation frequency is determined by the natural frequency of a Helmholtz resonator formed by the necks within the orifices and the cavity between them.

The current understanding of whistling encompasses a large range of underlying mechanisms that vary according to the characteristics of each system. Despite these differences, all mechanisms seem to share a fundamental requirement, which involves the presence of a feedback loop to sustain oscillations. Chanaud [15], in one of the first systematic classifications of whistling mechanisms, organized them in three distinct classes according to the nature of the feedback loop. The first class corresponds to purely hydrodynamic feedback, in which vortex formation and maintenance arise solely from flow-obstacle interactions. Aeolian tones generated by bluff bodies in a cross flow, such as power lines, airfoils or tree branches are characteristic examples [16–19].

The second class involves the presence of an acoustic feedback, occurring when an unstable jet interacts with a solid object. This interaction produces sound of dipole character, which propagates upstream and reinforces the jet instability. Examples include edge tones [20–22], hole tones [23–26], ring tones [27,28], pipe tones [29] and Rossiter modes in open cavities, such as found in aircraft slats [30–32].

The third class incorporates the presence of a resonator. In this case, the acoustic energy generated by the jet-structure interaction is trapped within the resonator's acoustic modes, whose dominant frequencies drive the jet instability. Typical examples include wind musical instruments such as flutes, recorders and the organ pipes [33–36]. An important aspect of this third class is the non-compact nature of the resonators involved.

A few years later, Wilson et al. [37] proposed an alternative classification of whistling based on the symmetry of the flow instability. In this scheme, asymmetric instabilities, such as the von Kármán vortex streets in planar jets, appear in edge tones and wind instruments. In contrast, symmetric instabilities, like the vortex rings in circular jets, occur in pipe tones and hole tones.

Building up on Rayleigh's explanation of hole tones, they hypothesized that human whistling is produced by a cavity formed between two smooth orifices: the first (upstream) created by the tongue pressing against the palate, and the second (downstream) formed by the lip constriction. This hypothesis was supported by an experimental parametric study using different cylindrical cavities separated by two smooth orifices. More recently, MRI and radiographic imaging of human subjects during whistling have confirmed this anatomical configuration [38].

However, an intriguing observation made by Wilson et al. [37] is that the jet instabilities, manifesting as vortex rings generated downstream of the first orifice, tend to dissipate before reaching the second orifice. In fact, by inserting a metallic wool inside the cavity and feeding the system with the same flow conditions, they observed that whistling could still be heard at the same frequency. This finding challenges Rayleigh's feedback-loop explanation, which attributes the phenomenon to the interaction between vortices formed at the first orifice and the second orifice, as discussed previously.

Since Wilson et al. [37], only a few studies have examined the specific sound-generation mechanism of human whistling, characterized by symmetric jet disturbances and an acoustically compact resonator. Henrywood and Agarwal [25] investigated a similar process in steam kettle whsitles, identifying two regimes depending on the Reynolds number (using the diameter of the orifice as the characteristic length). For $Re < 2000$, the whistling frequency was constant, set by the Helmholtz resonance of the whistle's cavity and orifice necks. For $Re > 2000$, the frequency scaled with the flow velocity (constant Strouhal number), determined by vortex shedding from the downstream orifice and determined by the flow-dependent resonance of an upstream tube.

In their study, the cavity length-to-orifice diameter ratio, L/d, ranged from 2.5 to 4.3, while the orifice diameter-to-plate thickness ratio was fixed at $d/t = 3$. These geometric parameters differ markedly from those observed in human whistling, for which L/d is significantly larger (≈ 10) and d/t is much smaller (≈ 0.5), as previously reported [37,38]. Furthermore, human whistling involves smooth orifice contours, in contrast to the sharp-edged geometries typical of steam kettle whistles.

Several studies have investigated whistling mechanisms in cavity-orifice systems and related vocal-tract configurations. Vovk et al. [39] numerically analyzed a viscous, incompressible flow through a cavity with ducts connected upstream and downstream, showing that self-sustained oscillations arise due to recirculation inside the cavity. This recirculating flow establishes a hydrodynamic feedback loop that generates vortex rings and periodic forcing at the second orifice, with two stable oscillation modes observed at constant Strouhal number. Longobardi et al. [26] examined the role of compressibility in a tone-hole configuration using global stability analysis, demonstrating that compressibility significantly increases growth rates and lowers oscillation frequencies, even at low Mach numbers. In the context of human whistling, Mori and Fukuda [40] attributed deviations between theoretical Helmholtz and whistling frequencies to the glottal opening, which increases upstream inertance. These results align with those discussed by Henrywood et al. [25]. Later, Mori et al. [41] investigated the difference between puckered and hollow whistling.

Table 1
Internal parameters of the Helmholtz resonators presented in Fig. 1a.

Resonator	L [m]	Volume [m^3]	d/t	L/d
A	3.80×10^{-2}	80.4×10^{-6}	0.5	6.0
B	6.35×10^{-2}	13.4×10^{-5}	0.5	10.0
C	8.89×10^{-2}	18.8×10^{-5}	0.5	14.0

They found that the former is driven by the vocal tract formants, whereas the latter is governed by the vocal tract's Helmholtz resonance.

Despite these advances, the feedback mechanism resulting from the interaction between the bias flow and the acoustic field inside the resonator is not yet fully understood. A more comprehensive description of this flow-acoustic coupling is therefore required to clarify the onset, sustainability and extinction of self-excited oscillations in such systems. The objective of this paper is to advance the understanding of the self-sustained oscillation mechanism underlying human whistling by providing a detailed description of the associated flow-acoustic feedback loop, including the pressure thresholds for oscillation onset and extinction. This is achieved through a combined experimental and analytical approach. The internal flow field in whistle geometries representative of the human vocal tract is characterized using particle image velocimetry (PIV), while simultaneous measurements of the acoustic field inside and outside the resonator are used to identify the regions and mechanisms responsible for sound generation.

To complement the experimental observations, a time-domain, analytical lumped-parameter model is developed in which the acoustic response of the resonator is coupled to a nonlinear self-excited oscillator of van der Pol type representing the hydrodynamic forcing induced by vortex shedding. This empirical model captures the essential features of the feedback loop, including the phase-dependent energy transfer between the flow and the acoustic field and the nonlinear saturation that limits the oscillation amplitude, thereby providing a physical framework for interpreting the experimental results.

This paper is structured as follows. Section 2 describes the whistle geometries investigated and the experimental methodology, including the acoustic measurements and the particle image velocimetry setup used to characterize the internal flow field. Section 3 presents the experimental results, with particular emphasis on the spectral characteristics of the acoustic response and the spatial organization of the velocity, vorticity, and coherence fields inside the resonator. In Section 4, an analytical lumped-parameter model of the whistle is introduced, coupling the acoustic dynamics of a double-neck Helmholtz resonator with a nonlinear van der Pol oscillator representing the hydrodynamic source. The model predictions are then compared with the experimental observations and used to interpret the onset, saturation, and extinction of self-sustained oscillations. Finally, Section 5 summarizes the main findings and discusses their implications for the understanding of human whistling mechanisms.

2. Experimental and numerical procedures

2.1. Physical models

This work builds on the experimental investigation conducted by Wilson et al. [37], which, to the best of our knowledge, remains the only study to address the feedback mechanism in human whistling with geometric parameters comparable to those observed in human whistling [38].

Accordingly, three resonator geometries analogous to those employed in their study were adopted here. However, unlike the original configurations, which featured circular cross sections, the present models were designed with a constant square cross section of side $h = 46$ mm in order to facilitate flow visualization and minimize the refractive parallax effects associated with curved resonator walls. The remaining parameters, including the three cavity lengths, L, the cavity volumes, V_c, the cross-sectional area, $A = 21.1 \times 10^{-4}$ m^2, the orifice plate thickness, $t = 12.7$ mm, and the orifice diameter, $d = 6.35$ mm, were identical to those considered by Wilson et al. [37]. The geometrical properties of the resonators are summarized in Table 1.

Fig. 1a shows a picture of the physical resonator models considered in the present study, while Fig. 1b provides a schematic drawing of the entire plenum/resonator system. To minimize the influence of upstream acoustic resonances, each resonator was mounted on a cubic plenum with dimension $D = 0.1$ m, which corresponded to an internal volume of 1.0×10^{-3} m^3. In addition, the upstream section of the plenum was connected to a divergent diffuser with an internal volume of 6.66×10^{-4} m^3, through which flow was introduced. The diffuser was lined with an acoustic-absorbing foam (melamine) to reduce sound reflections. A metallic rectifying mesh separating the diffuser and the plenum was introduced to reduce turbulent flow upstream from the resonator.

The back and bottom walls of each resonator, as well as the upstream and downstream plates containing the orifices, were manufactured by additive manufacturing using a resin printer with a dimensional precision of 17 μm. The front and top walls were constructed from 6 mm thick tempered glass. To minimize light reflections during the experiments, all internal walls, except the transparent front, were coated with matte black paint. In order to allow the laser light sheet to access the cavity, a longitudinal transparent slit was left uncoated on top wall of the resonators, as illustrated in Fig. 1a.

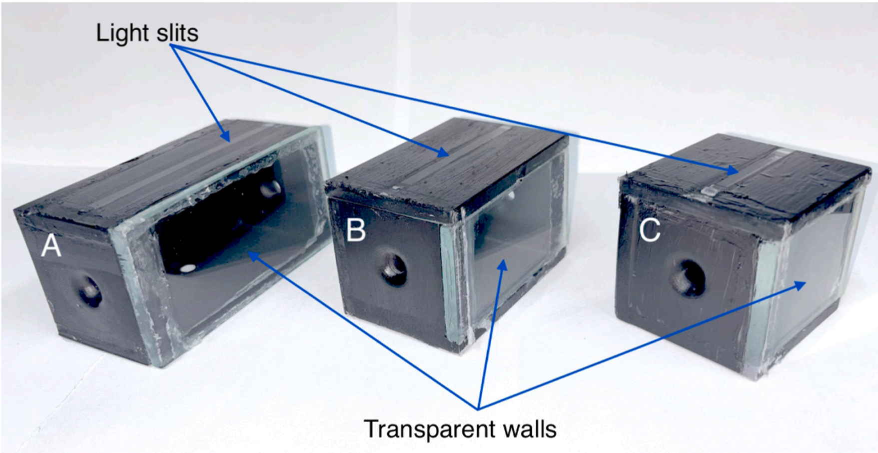

(a)

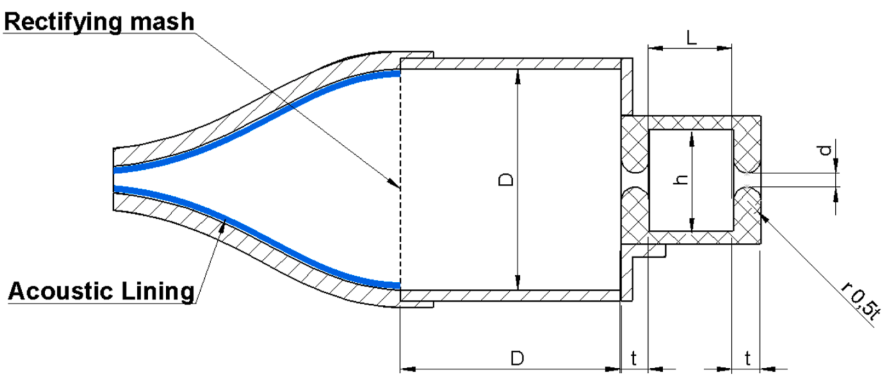

(b)

Fig. 1. Resonators/plenum arrangement. Fig. 1a Helmholtz resonators considered in the experiment; Fig. 1b Longitudinal section representation of the plenum/resonator coupling.

2.2. Experimental setup

Fig. 2 presents a schematic of the experimental apparatus. Time-resolved visualizations of the flow within the resonator cavities and at the outlet were acquired synchronously with the acoustic pressure inside and outside the resonator, as well as the static pressure within the plenum.

Acoustic measurements were conducted using two 1/4-inch pressure-field microphones (Brüel & Kjær Type 4944A) sampled at 8192 Hz. The internal acoustic pressure was measured by flush-mounting the first microphone on the bottom wall of the cavity, while the external acoustic pressure was recorded by positioning the second microphone along the sideline of the downstream orifice, perpendicular to the issuing jet at a distance of 30 mm. At each measurement, the static pressure inside the plenum was monitored with a differential pressure transducer (Omega PXM-409-070HGV). Both microphones and pressure transducer were interfaced with a data acquisition system (Brüel & Kjær Pulse LabShop, model 21/0/0.567).

Time-resolved particle image velocimetry (PIV) measurements were performed using a high-speed camera (Phantom Miro Lab 310) equipped with a 100 mm macro lens (Zeiss Milvus 2/100 mm), synchronized with a pulsed Nd:YLF laser (Litron LDY303). Synchronization was achieved via a dedicated timing unit (IDT type XS-TH), which also provided a TTL trigger for the acoustic and pressure data acquisition system. The PIV system was controlled using the commercial software Dantec DynamicStudio (Version 6.9).

The volumetric flow rate was regulated upstream of the seeder with a manual globe valve and monitored downstream using a parallel-plate laminar flow meter (Omega FMA-1611A), as illustrated in Fig. 2. The inflow of the plenum was seeded with di-ethylhexyl

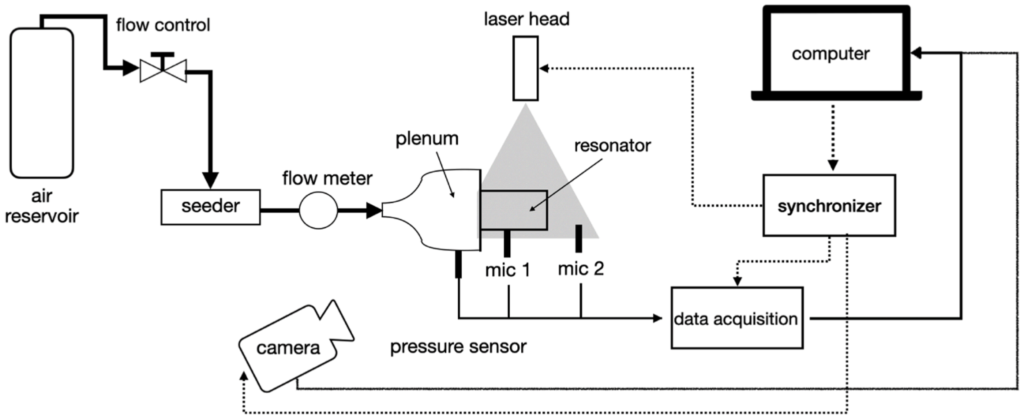

Fig. 2. Schematics of the experimental setup.

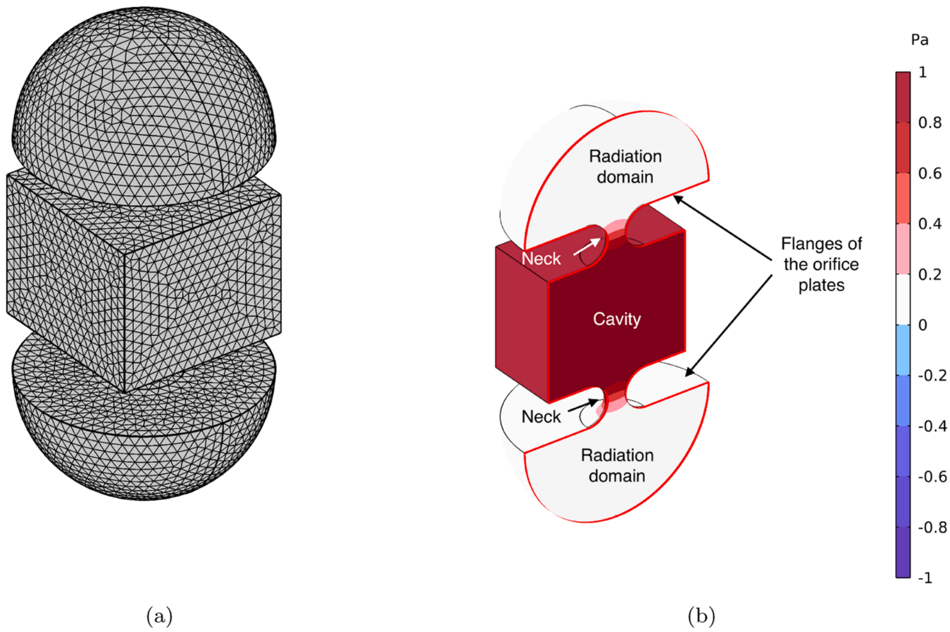

Fig. 3. Finite element model of Resonator A. Fig. 3a Illustration of the FEM mesh; Fig. 3b Longitudinal section of the model depicting the symmetric pressure distribution between necks, corresponding to Helmholtz mode at $f_H = 463.3$ Hz.

sebacate (DEHS) droplets generated by an atomizer equipped with six Laskin nozzles, producing a nearly uniform spatial distribution of tracer particles within the test section. Seeding conditions were adjusted to achieve an average of approximately 15 particles per interrogation window, ensuring sufficient image density. The mean particle diameter was approximately 1 μm, providing adequate flow tracking under the present experimental conditions and negligible inertial effects.

The histories of the velocity field within each resonator cavity were assessed by adjusting the camera frame rate at 4803 Hz, with a laser pulse interval between frame pairs of 20, 30 and 40 μs for resonators A, B and C, respectively, delivering 17 mJ per laser pulse. To ensure statistical convergence, 8166 image pairs were acquired at each measurement, corresponding to 2 s.

Post-processing was carried out using the PIVlab package (Version 3.09) for Matlab [42]. Each image pair was analyzed within a region of interest (ROI) of 361×436 pixels, corresponding to an area of 38×45.8 mm and an image resolution of 9.5 pixels/mm. Using interrogation windows of 16×16 pixels and assuming a maximum flow velocity of 14 m/s, the setup resulted in an average particle displacement of 2.66 pixels.

The images were processed with a multi-pass FFT window-deformation algorithm, employing 50% overlap. Three passes were performed to reach the final interrogation window size of 16×16 pixels. A velocity-based outlier detection was applied to the resulting vector field, yielding a valid detection probability (VDP) of 98.3%.

2.3. Finite element model

Before carrying out the experiments described in Section 2, the Helmholtz resonance frequencies, f_H, of resonators A, B, and C under quiescent conditions were computed using finite element simulations in COMSOL Multiphysics. The cavity and neck of each resonator were modeled with acoustically rigid walls. Free-field radiation was represented by hemispherical domains attached to each neck, with perfectly matched layers (PMLs) applied at their outer boundaries to suppress spurious reflections, following guidelines presented in previous studies [43,44]. Fig. 3 illustrate the FEM mesh used to compute f_H of Resonator A (Fig. 3a), as well as the Helmholtz (symmetric) mode of the same resonator at $f_H = 463.3$ Hz (Fig. 3b).

Eigenfrequency analyses were performed to obtain the resonance frequencies corresponding to the Helmholtz modes of each resonator. The meshes contained approximately 494 elements per wavelength at the highest frequency of interest, with local refinement in the neck to resolve steep pressure gradients. Mesh convergence was confirmed, as further refinement produced negligible changes in f_H. The computed Helmholtz frequencies, together with the experimental results discussed later, are summarized in Table 2. The computed eigenfrequencies will be compared with the self-sustained oscillation frequencies assessed experimentally and used to compute the neck's end correction based on the analytical model for the eigenfrequencies of double-neck Helmholtz resonators, proposed by Papadakis and Stavroulakis [45].

3. Experimental results

The following experiments were conducted in a laboratory environment with acoustic treatment, rather than in an anechoic chamber, with a minimum distance of 1.5 m between the resonator and surrounding surfaces. Nevertheless, the high sound pressure levels generated during self-sustained oscillations and the short distance between external microphone and the downstream orifice ensured a high signal-to-noise ratio throughout the measurements.

Moreover, the analyses presented hereafter rely primarily on spectral peaks, coherence, and cavity pressure measurements, which are governed by local resonator dynamics and are therefore expected to be only weakly affected by room reflections. Although reflected waves may slightly influence the measured SPL amplitudes, particularly from microphone 2, they are not expected to alter the identification of oscillation regimes, scaling relations, or the interpretation of the hydrodynamic-acoustic feedback mechanism.

Fig. 4 provides the experimental assessments, in black color, of the self-sustained oscillation frequencies measured outside the cavity (microphone 2) as a function of the Reynolds number, $Re = U_j d/\nu$, for the three resonators examined in this study, where U_j denotes the mean velocity of the jet in the upstream orifice and ν the kinematic viscosity of the air under normal conditions of temperature and pressure (NTP, 20 C^o and 1 atm). The results are compared with those reported by Wilson et al. [37] (in gray color), who investigated resonators with the same cavity volume, orifice plate geometry, and orifice diameter. The only distinction lies in the cavity cross section, which is circular in the latter case and square in the former, to facilitate improved PIV visualization. The blue horizontal lines indicate the Helmholtz frequency in the absence of the mean flow, f_H, obtained with eigenfrequency analyses based on the FEM model previously discussed.

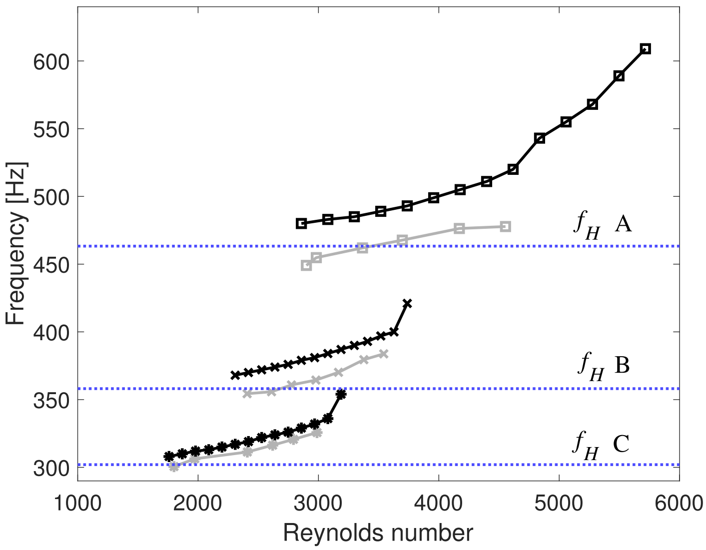

Fig. 4. Comparison between current measurements (black) and the results of Wilson et al. (1971, light grey) for detectable frequencies of self-sustained oscillation as a function of the Reynolds number. The blue dotted lines represent the Helmholtz frequency f_H computed for each resonator. □, ×, and ∗ correspond to resonators A, B, and C, respectively. (For interpretation of the references to colour in this figure legend, the reader is referred to the web version of this article.)

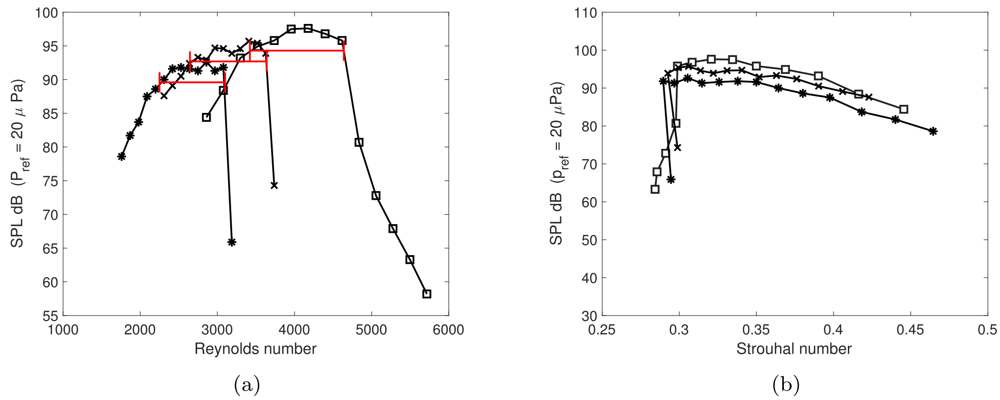

Fig. 5. Experimental results of the sound pressure level captured with microphone 2 as a function of the Reynolds number Fig. 5a, and as a function of the Strouhal number Fig. 5b. □, ×, and ∗ correspond to resonators A, B, and C, respectively. The red bars in Fig. 5a indicate the Reynolds number subregion beyond which the acoustic power decreases to half of its maximum value. (For interpretation of the references to colour in this figure legend, the reader is referred to the web version of this article.)

The agreement with the experimental results [37] is excellent for resonator C, but the discrepancy increases as the resonators decrease in volume. This deviation arises from the experimental procedure employed by Wilson et al. [37], in which the cavity volume was adjusted by varying the axial position of the downstream plate relative to the upstream one. For small resonators, this adjustment introduced a duct segment downstream of the second orifice, whose length was inversely proportional to the cavity length L. The presence of the additional duct segment downstream from the second orifice acts to effectively increase the inertance of the resonator neck, thereby reducing the resonator's characteristic frequency. A similar phenomenon has been reported by Henrywood and Agarwal [25] when investigating the influence of an upstream duct on the behavior of kettle whistles. Another expected feature of Fig. 4 is that the self-sustained oscillation frequency approximates to the computed Helmholtz frequency f_H (no flow) in the low Reynolds limit for all resonators.

A further insight of the results presented in Fig. 4 can be obtained when comparing them with those depicted in Fig. 5, which present the sound pressure level (SPL) measured outside the resonator's cavity (Microphone 2) as a function of the Reynolds number (Fig. 5a) and as a function of the Strouhal number (Fig. 5b). In what follows, the Strouhal number is defined as $St = fd/U_j$, where f is the peak frequency of self-sustained oscillation assessed with a discrete Fourier transform (DFT) of the time-domain pressure signal captured by Microphone 2.

The results shown in Fig. 5a demonstrate that the average SPL within the self-sustained oscillation region exhibits an inverse dependence on the cavity length L. For each curve in Fig. 5a, a subregion of Reynolds numbers was identified at the half-power level (i.e., 3 dB below the corresponding peak), beyond which self-sustained oscillations remain detectable, albeit with a pronounced decrease in SPL. These regions are indicated with red bars. Furthermore, the width of these half-power regions becomes narrower for longer cavities. The exact half-power Reynolds ranges of each resonator are provided in Table 2.

Fig. 5b reveals a clear scaling of the self-sustained oscillation regions with the Strouhal number, St, indicating that the characteristic dimension d is the dominant parameter governing the self-sustained oscillation dynamics of the present resonators. These results are consistent with the nondimensional analysis reported by Henrywood and Agarwal [25]. Furthermore, all resonators exhibit a pronounced peak at $St \approx 0.32$, a value that is in good agreement with previous experimental [25,37] and numerical [39] studies.

The dependence of the Strouhal number on the Reynolds number is illustrated in Fig. 6. Although the frequency exhibits an approximately linear relationship with Re as shown in Figs. 4 and 6a reveals that the Strouhal number varies significantly with Reynolds number. This behavor contrasts with those presented by Henrywood and Agarwal [25], who identified two distinct self-sustained oscillation regimes: at low Reynolds numbers, they found St to be inversely proportional to Re (corresponding to a constant-frequency region), while for $Re > 2000$, the Strouhal number remained approximately constant. In the present experiments, only the first regime was observed. This discrepancy is likely related to geometric differences between the whistles analyzed in each study, particularly the ratio L/d. In the present work, L/d ranged from 6 to 14, whereas in their study it varied between 2.5 and 4.3. In this sense, the constant-Strouhal regime reported by Henrywood and Agarwal appears to correspond more closely to that of a hole tone [23–26] or that of a pipe tone [29] rather than that of a long-cavity whistle.

An interesting feature of Fig. 6b is that the data collapse onto a single curve when plotted against the modified Reynolds number $Re_m = U_j\sqrt{Ld}/\nu$. This scaling indicates that the characteristic dynamics of the system are not governed solely by the diameter of the orifices d, but rather by a combined geometric length scale proportional to $\sqrt{Ld}$, suggesting a coupled influence of both the streamwise development length and the jet thickness on the flow behavior. Physically, this also suggests that the relevant balance between inertial and viscous effects is controlled not only by a purely local scale d, as observed by Henrywood and Agarwall [25], but also by how the flow evolves along the cavity or channel.

Based on the data presented in Fig. 6b, an empirical relationship between the global dependence of the Strouhal number on the modified Reynolds number was obtained by performing a least-squares polynomial regression using Matlab, yielding the following

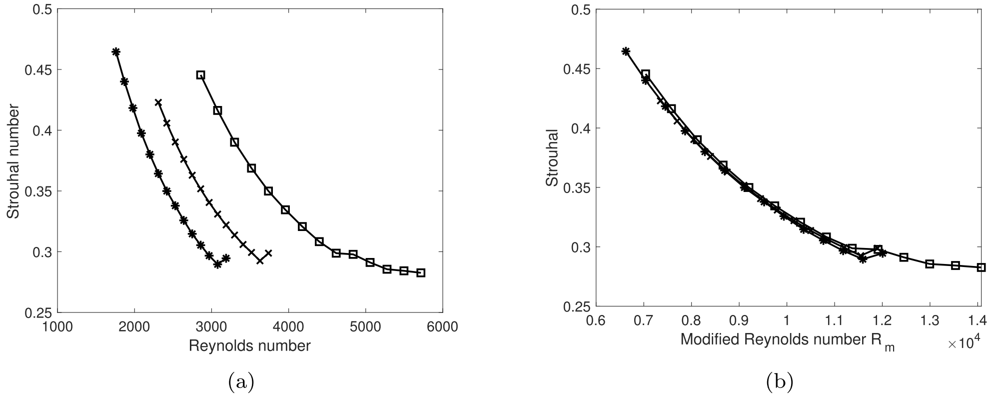

Fig. 6. Experimental Strouhal number as a function of Fig. 6a Reynolds number and Fig. 6b modified Reynolds number within the self-sustained oscillation regime. Symbols □, ×, and ∗ represent resonators A, B, and C, respectively.

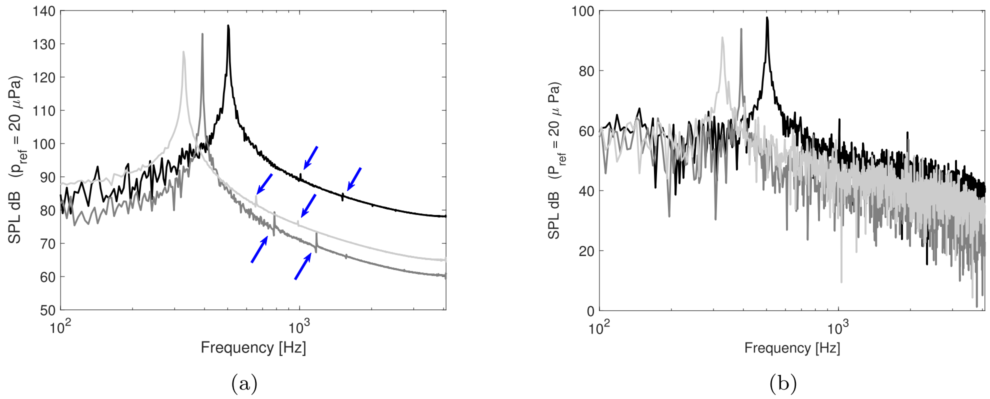

Fig. 7. Sound pressure level measured inside the resonator's cavity (Fig. 7a) and outside the downstream orifice (Fig. 7b). Resonators A, B and C are indicated by colors black, gray and light gray, respectively. The blue arrows in Fig. 7a indicate the presence of higher harmonics in each curve. (For interpretation of the references to colour in this figure legend, the reader is referred to the web version of this article.)

empirical expression

$$St = 697.4 Re_m^{-0.832}. \tag{1}$$

This expression, which holds only for the regions of self-sustained oscillation, will be used to estimate the vortex-shedding frequency of the analytical model discussed in Section 4.

Fig. 7 presents the sound pressure level spectra obtained inside (Fig. 7a) and outside (Fig. 7b) the resonators cavities. The results for each resonator correspond to the Reynolds value at which the maximum SPL is detected, according to Fig. 5a. The peak frequency and corresponding jet velocity associated to each curve are summarized in Table 2. An interesting feature of the spectra shown in Fig. 7a is the appearance of harmonics generated by nonlinear saturation, which naturally distorts the oscillatory waveform and transfers energy from the fundamental oscillation to higher-order harmonics. The higher-order harmonics in each curve are indicated by blue arrows.

To examine the difference in sound pressure level between internal and external microphones, Fig. 8 presents the sound pressure level difference, ΔdB, as a function of the Strouhal number. The results indicate an approximately constant relationship within the self-sustained oscillation region ($0.3 \lesssim St \lesssim 0.4$), with an averaged value of about 37 dB. This finding suggests that a substantial portion of the acoustic energy is generated within the resonator cavity, rather than being dominated by jet instabilities downstream of the second orifice, as implicitly assumed in previous works [15,25,27,46]. This interpretation is further supported by PIV results discussed in the following.

Fig. 9 presents the differential static pressure inside the plenum, relative to ambient atmospheric pressure, as a function of the Reynolds number for each resonator. As expected, the plenum pressure scales quadratically with the incoming flow velocity. Moreover, the similarity between the curves, particularly within the Reynolds range for self-sustained oscillation, indicates that the resonator geometry does not have a significant effect on the pressure build-up within the plenum, suggesting that the time-averaged pressure losses, primarily associated with vortex shedding, viscous dissipation, and acoustic radiation, are largely independent of the resonator volume.

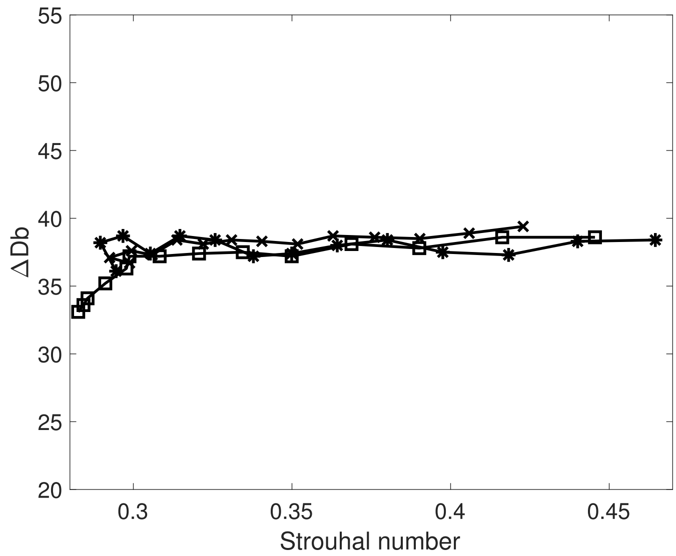

Fig. 8. Sound pressure level difference between internal and external microphones as a function of the Strouhal number within the regions of self-sustained oscillation. □, ×, and ∗ correspond to resonators A, B, and C, respectively.

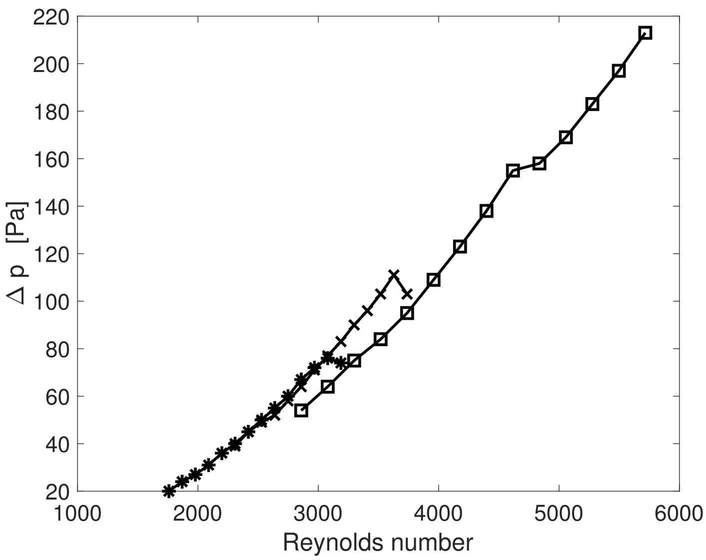

Fig. 9. Differential pressure in the plenum with respect to the atmospheric pressure as a function of the Reynolds number. □, ×, and ∗ correspond to resonators A, B, and C, respectively.

To assess the repeatability and reliability of these acoustic measurements, all reported SPL and their respective peak frequency values were obtained from averages over 100 independent records, each with a duration of 2 s. This averaging procedure substantially reduced the influence of random fluctuations associated with turbulence and background noise, resulting in highly stable spectral estimates and frequency identification.

A synthesis of the results obtained so far is summarized in Table 2.

3.1. Feedback-loop mechanism

The experimental results of the velocity field within the resonators obtained with the PIV technique described in Section 2.2 are presented in Figs. 10–12, corresponding to resonators A, B, and C, respectively. The streamwise velocity component, u, is shown on the left columns of each Figure, while their corresponding out-of-plane vorticity fields are displayed on the right. Each velocity map includes an inset indicating the instantaneous acoustic pressure phase inside the cavity, as measured by microphone 1.

To isolate the dominant tonal component at the frequency f of maximum amplitude, a digital band-pass filter was applied to the measured velocity and vorticity signals. The filter was implemented as an 8th-order infinite impulse response (IIR) design, with half-

Table 2
Summary of experimental and FEM results.

Resonator	$\mathbf{f_H}$ (FEM) [Hz]	Frequency at max. SPL [Hz]	Max. SPL Mic 1 [dB p_{ref} = 20μ Pa]	Max. SPL Mic 2 [dB p_{ref} = 20μ Pa]	Plenum pressure [Pa]	Mean jet velocity [m/s]	Reynolds range
A	463.3	505.1	135.0	97.6	123.2	9.99	3422 - 4640
B	358.1	392.9	133.4	95.7	93.0	8.16	2645 - 3640
C	302.0	331.6	129.8	91.9	70.0	7.10	2250 - 3102

power cutoff frequencies of ±30 Hz centered around f. The filter coefficients were designed to ensure stability and a well-conditioned frequency response, and zero-phase filtering (forward-backward processing) was employed to prevent phase distortion. This procedure enabled accurate reconstruction of the amplitude and phase of the self-sustained oscillations while effectively suppressing pressure fluctuations at other frequencies.

The filtered velocity and vorticity fields clearly reveal the coherent flow structures responsible for the acoustic feedback mechanism. In particular, they highlight the periodic formation and convection of vortical structures in the jet region, which interact with the resonator cavity to sustain oscillations and radiate sound.

An important feature observed in Figs. 10–12 is the significant attenuation of vorticity as the vortex rings generated at the upstream orifice (orifice 1 - left side) convect toward the downstream orifice (orifice 2 - right side). This decay is particularly pronounced in Figs. 11 and 12, corresponding to Resonators B and C, respectively. Although Wilson et al. [37] did not report the complete disappearance of vortical structures as they propagated within the resonator, they hypothesized that vortices generated at the upstream orifice do not directly interact with the downstream orifice. This hypothesis was based on their experimental observation that inserting a metallic wool at the mid-length of the cavity, thereby inhibiting vortex convection, did not suppress the self-sustained oscillation. The attenuation observed in the present results is therefore consistent with their interpretation, suggesting a weak or negligible hydrodynamic coupling between the two orifices.

These results also suggest that the classical hydrodynamic-acoustic feedback mechanism hypothesized by Rayleigh [14], which rely on the interaction of coherent vortical structures with the second orifice, thereby generating pressure fluctuations that would reach back the first orifice and reinforce hydrodynamic instabilities, does not apply to the current whistles. Although this mechanism has been shown accurate in other whistling systems, such as the hole tone [25,27,46] and Rossiter tones [30–32], it is unlikely to be the dominant process in double-neck Helmholtz resonators with elongated cavities ($L/d > 5$) subjected to a low-Reynolds bias flow.

Instead, the feedback loop appears to be governed by a hydro-acoustic interaction localized within the cavity near the first orifice. In this case, the feedback loop seems to encompass the following stages: First, bias flow entering through the upstream neck develops shear-layer instabilities at the orifice edge, which subsequently roll up into a vortex ring. As this vortex grows and convects downstream from orifice 1 (Figs. 10d–12d), it induces an additional unsteady volumetric flow, Q_v, into the cavity. This process is evidenced by the pronounced red regions near orifice 1 in Figs. 10c–12c, indicating strong inward flow.

The additional flow injection causes the cavity pressure p_c to increase progressively. As expected from the resonator dynamics, the pressure does not reach its maximum simultaneously with the flow injection, but approximately one-quarter cycle later, as shown in the insets of Figs. 10e–12e. At this stage, the vorticity immediately downstream of orifice 1 becomes very weak (10f–12f), indicating that the vortex-induced unsteady flow has nearly vanished. Consequently, Q_v approaches zero near the orifice, as seen in Figs. 10e–12e.

Once the cavity pressure reaches its maximum, the pressure difference between inner and outer domains of the resonator begins to drive fluid outward through orifice 1. At the same time, as the initial positive vortex convects further downstream, a negative vortex starts to take place near the upstream neck (Figs. 10h–12h). This newly formed vortex induces a negative unsteady flow Q_v, which further enhances the outward motion through the orifice.

The outward flow through orifice 1 reaches its maximum approximately one-quarter cycle after the pressure peak. This stage is evidenced by the pronounced blue regions near the upstream orifice in Figs. 10g–12g, corresponding to strong flow leaving the cavity.

An important feature of this mechanism is the approximately 90-degree phase difference between the cavity pressure p_c and the vortex-induced flow Q_v. This behavior is described by the continuity-based relation

$$\frac{dp_c}{dt} = -K(Q_2 - Q_1 + Q_v), \tag{2}$$

where Q_1 and Q_2 represent the instantaneous acoustic volumetric flows through the upstream and downstream necks, respectively. These flows correspond to the oscillatory exchange of fluid driven by the acoustic response of the resonator. In contrast, Q_v represents the equivalent fluctuating volumetric flow induced by the vortex dynamics near the upstream neck and therefore acts as a hydrodynamic forcing term coupling the vortex shedding process to the cavity acoustics. The parameter $K = \rho_0 c_0^2 / V_c$ denotes the acoustic compliance coefficient of the cavity, where V_c is the cavity volume.

The resulting pressure fluctuations subsequently reinforce the shear-layer instability near orifice 1, promoting the formation of new vortices and thereby closing the hydrodynamic-acoustic feedback loop. Within this framework, self-sustained oscillations are maintained when the energy transferred from vortex shedding to the cavity exceeds the combined viscous and acoustic losses of the system, including radiation.

The downstream distance from orifice 1, at which the interaction between the acoustic field and the vortical structures is most intense can be estimated by adapting the empirical expression originally proposed by Rossiter [47], which defines the feedback-loop

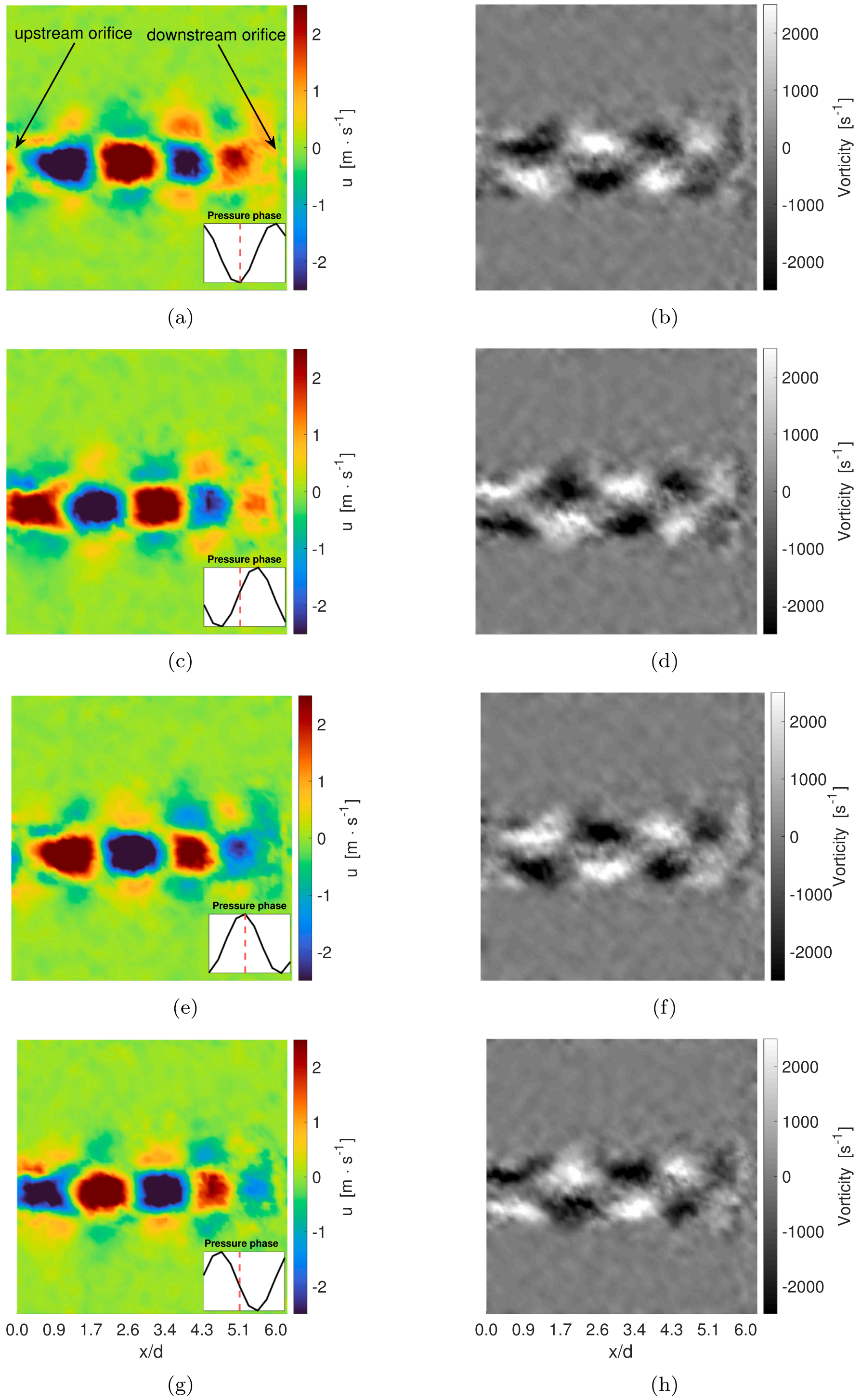

Fig. 10. Flow visualizations over one duty cycle for resonator A, obtained with PIV and band-pass filtered around the centre frequency of the self-sustained oscillation (505 Hz, ± 50 Hz). The left column shows the horizontal velocity component u, and the right column the corresponding out-of-plane vorticity $\boldsymbol{\omega}_z$. Insets in the velocity plots indicate the phase of the acoustic pressure for the corresponding duty cycle.

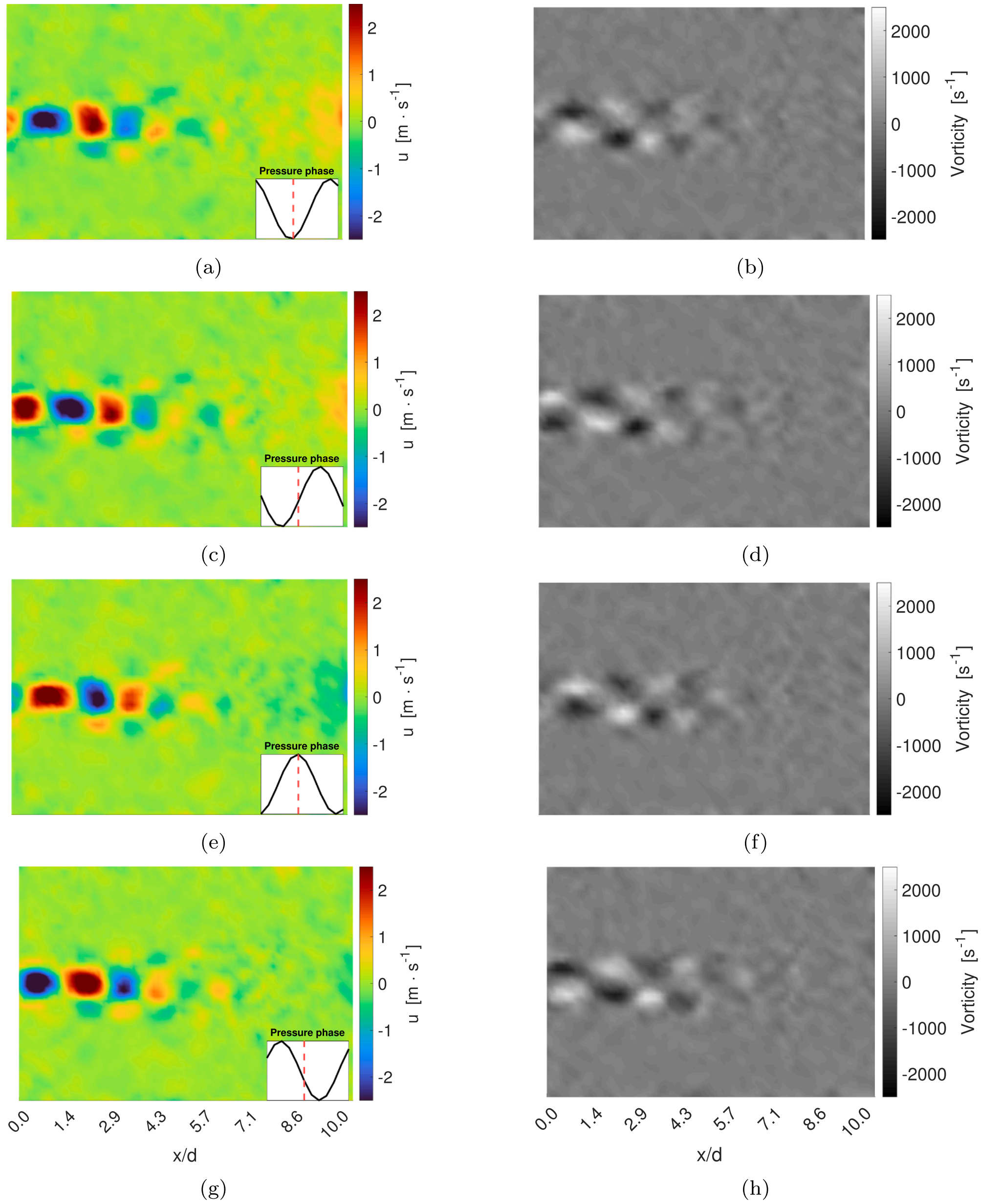

Fig. 11. Flow visualizations over one duty cycle for resonator B, obtained with PIV and band-pass filtered around the centre frequency of the self-sustained oscillation (393 Hz, ± 50 Hz). The left column shows the horizontal velocity component u, and the right column the corresponding out-of-plane vorticity $\boldsymbol{\omega}_z$. Insets in the velocity plots indicate the phase of the acoustic pressure for the corresponding duty cycle.

condition for shallow cavities, given by

$$n = f(t_{ac} + t_{conv}) + \gamma, \tag{3}$$

where f is the frequency of self-sustained oscillation, n is an integer representing the shear layer hydrodynamic instability mode and γ is the phase delay associated with vortex formation and scattering. Moreover, t_{ac} and t_{conv} are, respectively, the acoustic and hydrodynamic propagation times, given by

$$t_{ac} = \frac{\delta}{c_0 - U_j}, \tag{4}$$

and

$$t_{conv} = \frac{\delta}{U_j \kappa}. \tag{5}$$

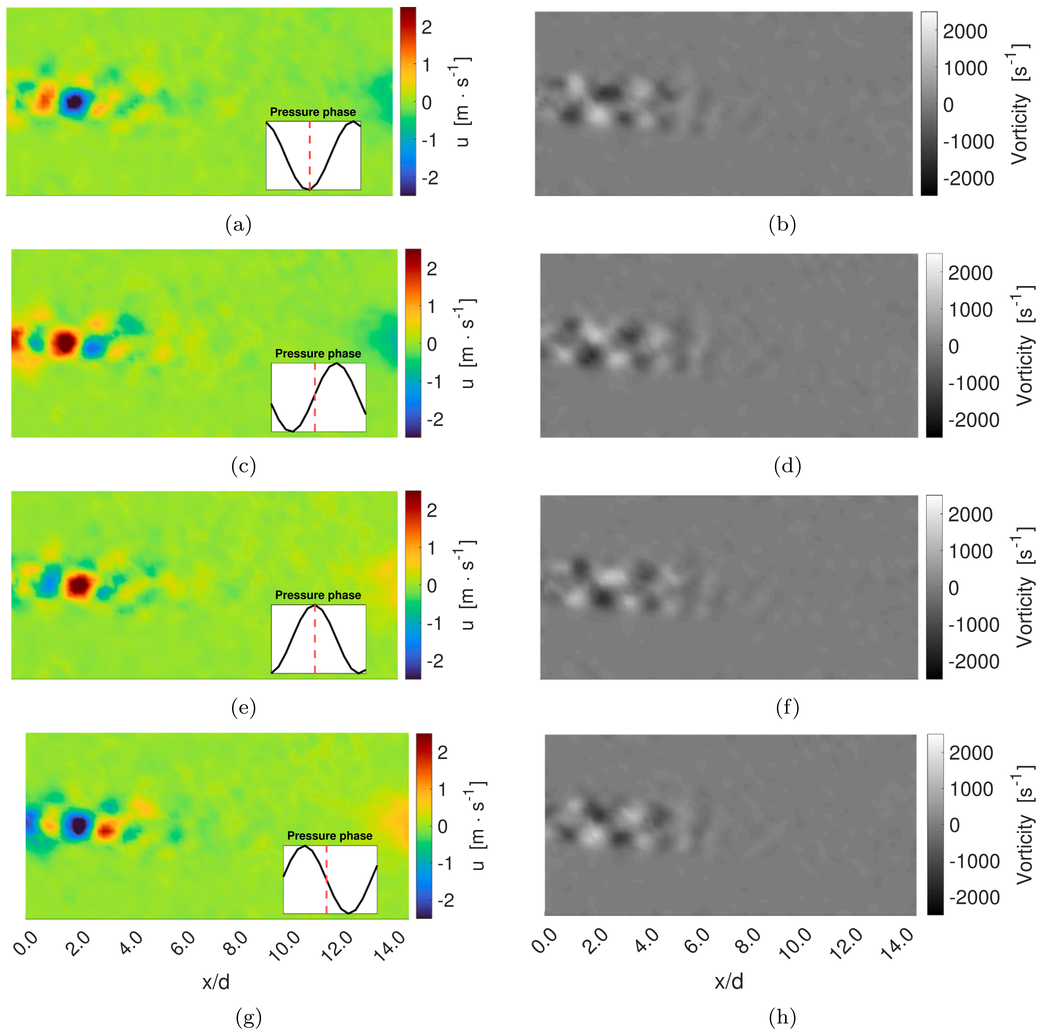

Fig. 12. Flow visualizations over one duty cycle for resonator C, obtained with PIV and band-pass filtered around the centre frequency of the self-sustained oscillation (331 Hz, ± 50 Hz). The left column shows the horizontal velocity component u, and the right column the corresponding out-of-plane vorticity $\boldsymbol{\omega}_z$. Insets in the velocity plots indicate the phase of the acoustic pressure for the corresponding duty cycle.

In both Eqs. (4) and (5), δ represents the characteristic distance at which the hydrodynamic-acoustic interaction takes place. κ in Eq. (5) is the ratio between vortex convection velocity, U_{conv}, and the mean jet velocity, U_j. Using the previous definition of the Strouhal number $St = fd/U_j$, Eq. (3) can be rearranged, so as to obtain the normalized distance δ/d by

$$\frac{\delta}{d} = \frac{n-\gamma}{St}\left(\frac{U_j}{c_0 - U_j} + \frac{1}{\kappa}\right)^{-1}. \tag{6}$$

Before calculating δ/d, a few remarks should be made. First, The phase term γ, is assumed to be zero in the case of a double-neck Helmholtz resonator, considering the vortex to be instantaneously formed at the beginning of a duty cycle. The velocity ratio κ was determined directly from the PIV data by tracking the evolution of the vorticity field using a space-time cross-correlation approach described by Dellano et al. [48]. The analysis was restricted to the centerline of the upper shear layer, where coherent vortical structures are most pronounced. Finally, the nominal distances δ/d at which the acousto-hydrodynamic interaction occurs were calculated for each resonator using Eq. (6), which yielded the values of 2.31, 2.30 and 2.28, for resonators A, B and C, respectively.

To augment the discussion involving these results, Fig. 13 present the cross-power spectral densities (CPSD) (Fig. 13a) and the two-point coherence (Fig. 13b) between the external acoustic pressure (Mic. 2) and the horizontal component of particle velocity, u, measured along the centerline of all resonators at the frequency of maximum SPL, considering the values provided in Table 2. Furthermore, Fig. 13c presents the spatial distribution of the vorticity averaged over time and normalized by U_j.

For all resonators, the maximum CPSD in Fig. 13a occurs at $x/d \approx 2.3$, as indicated by the vertical dashed line (in blue). As observed in Fig. 13b, the coherence is also notably high around this value. Interestingly, these values coincide with those obtained for the normalized distance δ/d that defines the feedback loop. These results indicate that most of the acoustic energy is being

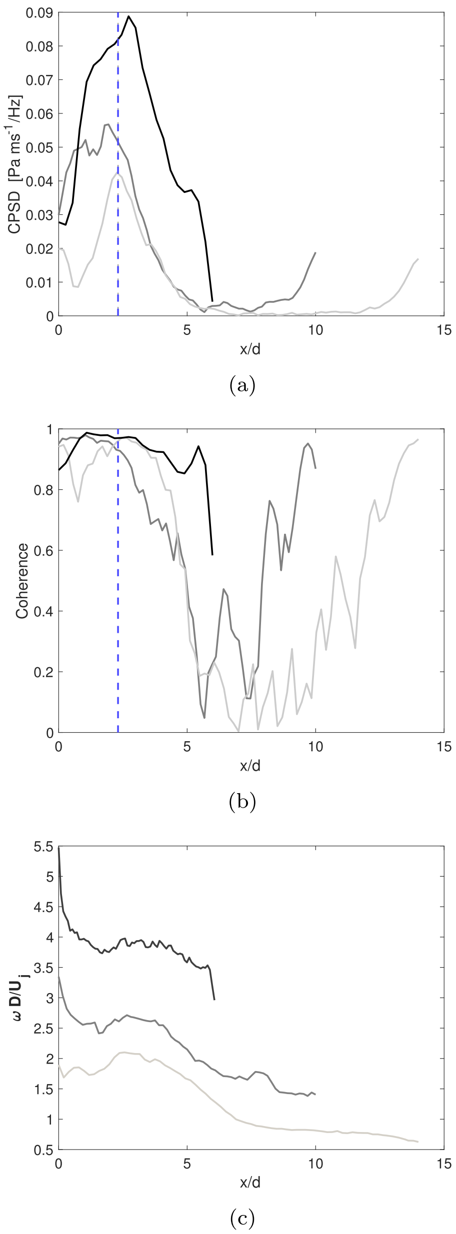

Fig. 13. Cross power spectral density (Fig. 13a) and coherence between external acoustic pressure (mic 2) and horizontal component of the particle velocity (Fig. 13b) and normalized average vorticity (Fig. 13c). The vertical dashed line (in blue) in Fig. 13a and b indicate the averaged x/d value around which the coherence peak occurs. The velocity values were obtained along the centerline of resonators A (black), B (gray), and C (light gray) at their center frequencies corresponding to 505 Hz, 393 Hz and 331 Hz, respectively. (For interpretation of the references to colour in this figure legend, the reader is referred to the web version of this article.)

produced inside the resonator at the distance $x/d \approx 2.3$. The normalized vorticity shown in Fig. 13c suggests that the first vorticity peaks occur immediately downstream of the first orifice, which is expected due to the strong shear between the jet and the orifice wall. However, second vorticity maxima emerge around $x/d \approx 2.3$, coinciding with the regions of maximum acoustic power generation shown in Fig. 14b and with δ/d.

To reinforce the hypothesis that most of the acoustic energy is generated inside the cavity, a similar analysis was carried out considering, at this time, a ROI encompassing both the internal and external velocity fields of Resonator A, as shown in Fig. 14.

As in the previous cases shown in Fig. 13 , the CPSD between particle velocity and external pressure attains its maximum within the resonator chamber, at approximately $x/d \approx 2.4$ from orifice 1. This reinforces the fact that most of the acoustic energy is generated inside the resonator rather than externally by coherent structures of the jet, as hypothesized by Chanaud et al. [27], and more recently by Henrywood and Agarwal [25].

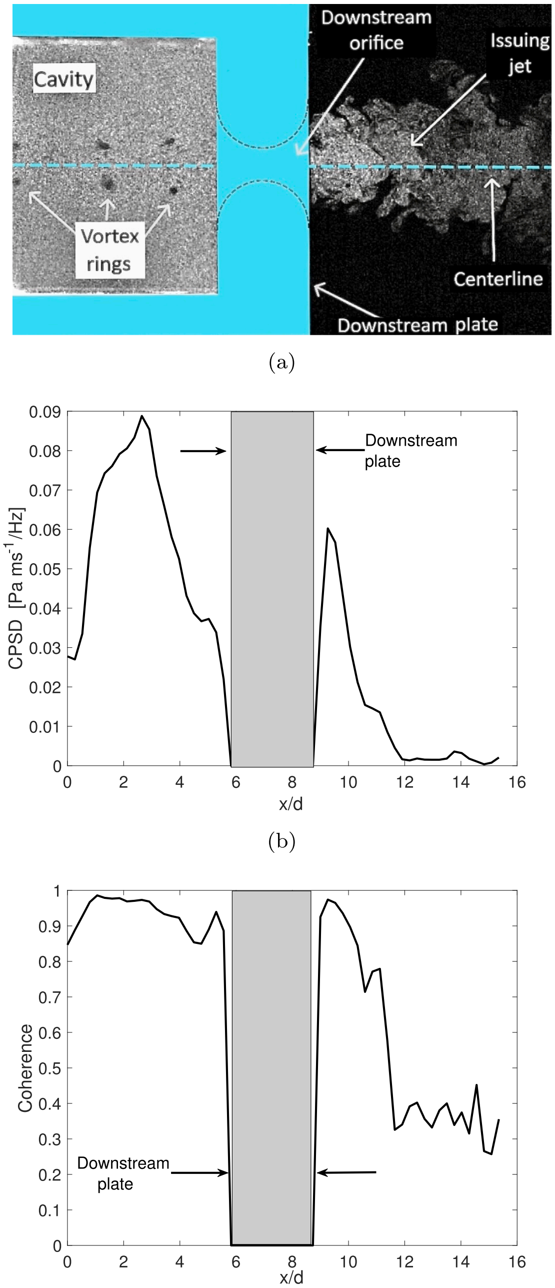

Fig. 14. Flow visualization (Fig. 14a), cross power spectral density (Fig. 14b) and coherence (Fig. 14c) between external acoustic pressure (mic 2) and horizontal component of the particle velocity along centerline for Resonator A at $f = 505$ Hz and $Re = 4132$.

The corresponding two-point coherence distribution between external acoustic pressure and the horizontal velocity component along the centerline is shown in Fig. 13c, which corroborates the CPSD results in Fig. 13b. Although the coherence remains high near the downstream regions of both orifices, the CPSD amplitude (Fig. 13b) reaches its highest values at $x/d \approx 2.5$.

To assure the repeatability and reliability, the coherence distributions and the corresponding identification of the acoustic source location presented above were verified through five independent experimental runs performed under the same operating conditions. All experiments produced essentially identical coherence patterns and source localization results, demonstrating a high degree of repeatability of the measurements and robustness of the conclusions.

These findings establish the physical framework upon which the subsequent analytical model is formulated, enabling a more detailed description of the observed hydrodynamic/acoustic coupling.

4. Analytical model

Before entering the description of the model, it is worth mentioning that the present lumped model developed in this work is not a first-principles predictive tool. Rather, its purpose is to capture the dominant nonlinear physical mechanisms governing self-sustained oscillations in whistle-like Helmholtz resonators driven by vortex shedding, and to rationalize experimental observations within an empirical, physically interpretable framework. The vortex dynamics are represented by a van der Pol-type oscillator augmented with circulation decay effects, while energy dissipation at the orifices is modeled through a nonlinear quadratic loss term.

The Van der Pol oscillator has been extensively employed to describe vortex-shedding dynamics. It was first introduced to model vortex shedding from stationary circular cylinders in cross-flow [49], later extended to represent instabilities in other configurations such as conical bodies [50], and more recently applied to capture nonsynchronous vibrations in turbomachinery induced by vortex shedding [51].

The present formulation relies on several simplifying assumptions. First, the cavity is considered acoustically compact with respect to the wavelength, $\lambda_H = c_0/f_H$, where f_H is the resonance frequency of the Helmholtz resonator in the absence of mean flow. Second, the pressure fluctuation within the cavity, p_c, is assumed to remain sufficiently small so that the cavity compliance can be treated as linear. Third, the flow through the necks is modeled as a quasi-steady incompressible jet, allowing the pressure drop at each neck, $p_{drop\ 1,2}$, to be expressed as a quadratic function of the volume flow, thereby accounting for flow separation and vena contracta effects. Finally, the flow injection induced by a vortex ring, Q_v, is assumed to be proportional to its circulation, Γ.

Under these assumptions, the double-neck Helmholtz resonator is represented by a two-degree-of-freedom lumped model, whose momentum balance equations are given by

$$\begin{aligned} M_1\frac{dQ_1}{dt} &= p_p - p_c - R_1 Q_1 - p_{\mathrm{drop},1},\\ M_2\frac{dQ_2}{dt} &= p_c - p_0 - R_2 Q_2 - p_{\mathrm{drop},2}. \end{aligned} \tag{7}$$

Here, and in what follows, the subscript $i = 1, 2$ refers to the upstream and downstream orifices, respectively. The quantities Q_i denote the unsteady volumetric flows through each orifice, while p_p and p_0 correspond to the prescribed upstream (plenum) and downstream (atmospheric) pressures.

The linear viscous losses in the necks with cross-sectional areas A_i, are represented by the viscous damping coefficients R_i. The acoustic inertances associated with the air slugs within the resonator necks are given by

$$M_i = \frac{\rho_0 L_{e_i}}{A_i}, \tag{8}$$

where

$$L_{e_i} = T/2 + a d_i, \tag{9}$$

denotes the effective neck length, T is the thickness of the orifice plate, which is halved in Eq. (9) because flow separation occurs at the location of maximum orifice constriction in the case of a symmetric bell-mouth-shaped orifice, shown in Fig. 1b.

The end-correction coefficient a in Eq. (9) is expressed as a fraction of the orifice diameter d and depends strongly on both the orifice geometry and the mean flow velocity [52,53]. In the present study, the orifices have identical diameters, so that $A_1 = A_2$, and $L_{e_1} = L_{e_2}$. The parameter a was estimated by using the Helmholtz resonance frequencies obtained from the FEM analyses in the absence of mean flow, presented in Table 2, with the analytical prediction for a symmetric double-neck Helmholtz resonator proposed by Papadakis et al. [45], given by

$$f_H = \frac{c_0}{2\pi}\sqrt{\frac{2A_1}{V_c L_{e_1}}}. \tag{10}$$

This procedure yielded a common value of $a = 0.72$ for all resonators, and is consistent with the values found for tubes terminated by flanges [44] and circular horns in the absence of a mean flow [54,55].

Assuming a quasi-steady, incompressible jet through each neck, the nonlinear pressure drop associated with jet formation and shear-layer instabilities is modeled as

$$p_{\mathrm{drop},i} = \frac{\rho_0}{2C_{d_i}^2 A_i^2} Q_i|Q_i|, \tag{11}$$

where the discharge coefficients C_{d_i} are set to 0.98, as expected for circular orifices featuring rounded inlet and outlet edges [56].

The cavity pressure, p_c, in Eq. (7) is assessed by resolving the pressure evolution given by Eq. (2), assuming mass conservation within the resonator.

As previously mentioned, the vortex-induced flow injection in the cavity is proportional to the vortex circulation, Γ, such that

$$Q_v = C_v \Gamma, \tag{12}$$

where C_v is a proportionality constant that can be interpreted as a characteristic length scale of the region where the vortex circulation induces a net volume flow, typically $\sim \mathcal{O}(d)$ [57]. Γ is obtained by resolving the time evolution equation given by

$$\frac{d\Gamma}{dt} = \alpha U_j \dot{q} - \frac{\Gamma}{\tau_d}, \tag{13}$$

Table 3
Summary of parameter values used in the analytical model.

Resonator	R_i [kg/m^{4}s]	C_v [m]	α [m]	τ_{d_0} [s]	γ [Pa^{-1}]	μ [1/s]	κ [m/kg]	β [s.m^{-1}]
All	1.0	1.3×10^{-3}	1.27×10^{-2}	5.0×10^{-3}	0.09	3.1	1	0.3

where $\dot{q}$ represents the vortex velocity in generalized coordinates, α is a scaling factor linking the vortex velocity $\dot{q}$ with circulation Γ, and τ_d is the circulation decay time. The scaling factor $\alpha \sim \mathcal{O}(U_j d)$ has a crucial role at determining the intensity of the feedback loop between the vortex and the cavity. A larger α corresponds to a stronger driving force due to the vortex flow injection, leading to stronger self-sustained oscillations.

The circulation decay time τ_d characterizes the timescale over which the vortex loses circulation due to viscous diffusion and secondary dissipative mechanisms, such as three-dimensional breakdown and vortex-cavity interactions. It depends on both the flow state Q_1 and the cavity pressure p_c. Larger values of Q_1 correspond to stronger shear, faster entrainment, and consequently smaller τ_d. Similarly, stronger acoustic oscillations within the cavity enhance unsteady shear and entrainment, also reducing τ_d. Based on these considerations, the circulation decay time is modeled as

$$\tau_d = \frac{\tau_{d_0}\exp(-\gamma|p_c|)}{1+\beta|Q_1/A_1|}, \tag{14}$$

where $\tau_{d_0} \sim \mathcal{O}(d/0.5U_j)$ is the baseline circulation decay time, β, and γ are empirical coefficients characterizing flow dependence, and pressure sensitivity, respectively.

The vortex velocity $\dot{q}$ in Eq. (13) is obtained by solving the forced van der Pol oscillator Equation, given by

$$\ddot{q} - \mu(1-q^2)\dot{q} + \omega_v^2 q = \kappa p_c. \tag{15}$$

Eq. (15) describes the periodic oscillation of the shear layer and the associated formation of vortex rings. The right-hand side represents the feedback from the cavity pressure p_c on the vortex motion. The nonlinear damping term $-\mu(1-q^2)\dot{q}$ changes sign with the instantaneous value of the state variable $q(t)$. For $|q|<1$, the damping term $-\mu(1-q^2)\dot{q}$ becomes negative, injecting energy into the system, whereas for $|q|>1$, it becomes positive, dissipating energy. The vortex frequency ω_v, is extracted from the Strouhal number $St=\omega_v d/2\pi U_j$, using the empirical expression given by Eq. (1).

The RHS of Eq. (15) represents the forcing of the hydrodynamic oscillator by the acoustic field given by the cavity pressure p_c. The parameter κ represents the strength of acoustic forcing on the hydrodynamic oscillator. It quantifies the sensitivity of the inlet shear layer to cavity pressure fluctuations and governs the conversion of acoustic energy into oscillatory jet motion, thereby closing the aeroacoustic feedback loop responsible for self-sustained oscillations.

Combining Eqs. (12) and (15) results in a coupled system that captures the bidirectional interaction between the cavity pressure p_c and the vortex-induced flow Q_v. As a result, p_c accounts for the influence of the acoustic field on the vortex dynamics, while Q_v represents the reciprocal effect of vortex motion, through Eq. (12), on the acoustic pressure in the cavity, p_c.

Table 3 summarizes the single set of model parameters adopted in this study. These parameters were determined empirically by calibrating the model predictions of the maximum SPL as a function of the Reynolds number against the corresponding experimental data. The calibration was performed only for Resonator B, after which the resulting parameter values were used as the single set for all resonators. Although identified empirically, each parameter corresponds to a distinct and physically meaningful mechanism governing vortex formation, convection, and decay, as well as their coupling with the acoustic field, as described previously. The obtained values lie within physically plausible ranges and exhibit consistent scaling with the relevant geometric and flow parameters.

The system of ODEs, namely Eqs. (2), (7), (13) and (15) was integrated in time domain using MATLAB's variable-step stiff ODE solver *ode15s*, which is based on backward differentiation. This method was chosen to ensure numerical stability and accuracy in the presence of the multiple time scales inherent to the problem, particularly the separation between the acoustic oscillation period and the slower circulation decay dynamics. The relative and absolute tolerances were set to 10^{-8} and 10^{-19}, respectively, to guarantee convergence of both the fast and slow components of the solution. Each simulation was initialized by prescribing the atmospheric pressure $p_0 = 0$ Pa and the plenum pressure, p_p, according to the range of values measured for each resonator, as presented in Fig. 9. Moreover, the initial values of Q_1, Q_2, q, $\dot{q}$ and Γ were set to zero at $t=0$.

The following Section compares analytical results with experimental data and discusses aspects of the feedback-loop mechanism based on the outcomes of the model.

5. Analytical results and discussion

Fig. 15 presents the results obtained with the analytical model, considering Resonators A, B and C at their maximum self-oscillation amplitude, which were achieved by imposing the plenum pressures presented in Table 2, while the atmospheric (downstream) pressure, p_0, was set to zero.

The left column of Fig. 15 illustrates the predicted time histories of the cavity pressure, p_c, normalized by the plenum pressure, p_p, for Resonators A (Fig. 15a), B (Fig. 15c), and C (Fig. 15e). The results illustrate the capability of model at capturing the transient and steady-state regimes, which is achieved after a short period of time, when the system response reaches saturation. Furthermore,

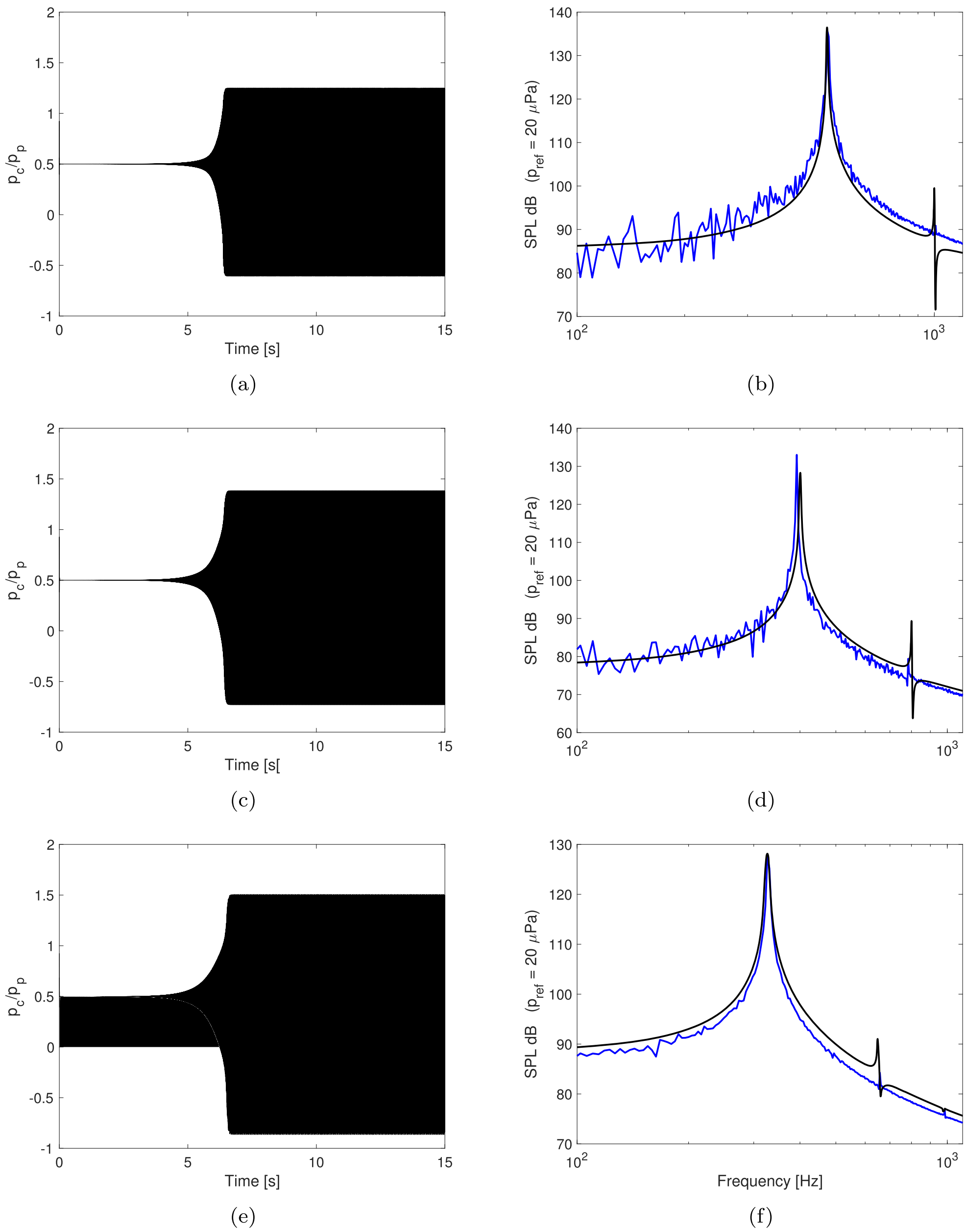

Fig. 15. Results for the cavity pressure, p_c at the maximum oscillation regime for Resonators A, B and C, according to the values presented in Table 2. Left column presents the predicted time histories of the normalized pressures for Resonators A (a), B (c) and C (e). The right column compares the SPL spectra for Resonators A (b), B (d) and C (f) obtained analytically (black) and experimentally (blue). (For interpretation of the references to colour in this figure legend, the reader is referred to the web version of this article.)

in all cases, the normalized pressure values indicate that the steady component of the cavity pressure is always half of the plenum pressure p_p.

The right column of Fig. 15 shows the cavity sound pressure level spectra (black curves) for Resonators A (Fig. 15b), B (Fig. 15d), and C (Fig. 15f). The spectra were obtained by applying a discrete Fourier transform to the corresponding time histories displayed in the left column, after removing the transient portions. The experimental results (blue curves) were obtained for the same resonators, using identical pressure conditions as those assumed in the model, namely $\Delta p = p_p - p_0$.

The close agreement between the predictions and the experimental data demonstrates that the model accurately captures the resonator dynamics during self-sustained oscillations. Another noteworthy feature is the presence of secondary peaks in both the predicted and measured spectra, which are likely associated with harmonic generation arising from nonlinear saturation. Such nonlinear effects naturally distort the waveform and transfer energy from the fundamental oscillation to higher harmonics.

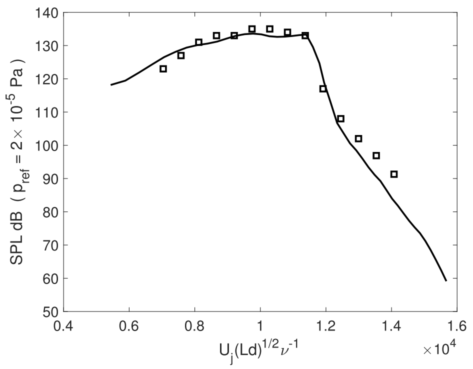

(a)

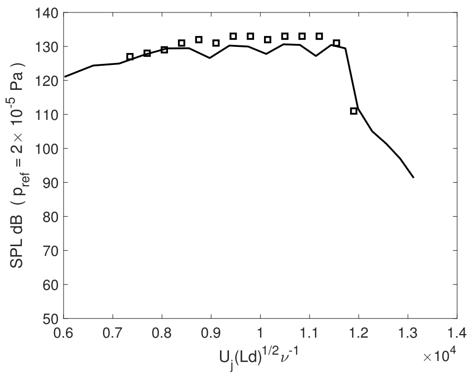

(b)

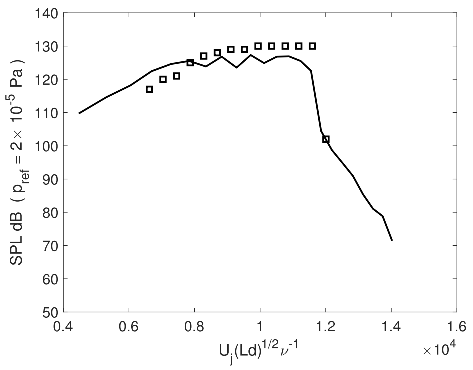

(c)

Fig. 16. Comparison between analytical and experimental results for the maximum SPL as a function of the modified Reynolds number Re_m between oscillation onset and extinction (symbols: experiments; lines: analytical). Resonator A (16a), B (16b), and C (16c).

In the analytical model, this behavior is represented by the nonlinear hydrodynamic feedback introduced through the van der Pol oscillator. The appearance of similar secondary peaks in the experimental spectra supports the physical relevance of this mechanism and indicates that the model captures the essential nonlinear dynamics governing the self-sustained oscillation.

The overprediction of the secondary peaks by the analytical model in Fig. 15b, d, and f can be attributed to the fact that the model concentrates the nonlinear behavior into an idealized deterministic saturation term. In contrast, the real system involves additional dissipative and decoherence mechanisms, including turbulence, viscous and radiation losses, vortex irregularities, and spatial averaging effects, that preferentially attenuate higher-frequency components and redistribute part of the harmonic energy over a broader spectral range.

To evaluate the ability of the model to accurately capture both the onset and extinction of self-sustained oscillations, analytical predictions are compared with experimental results in Fig. 16 in terms of maximum SPL as a function of the Reynolds number, covering the range between the onset and extinction of self-sustained oscillations observed experimentally.

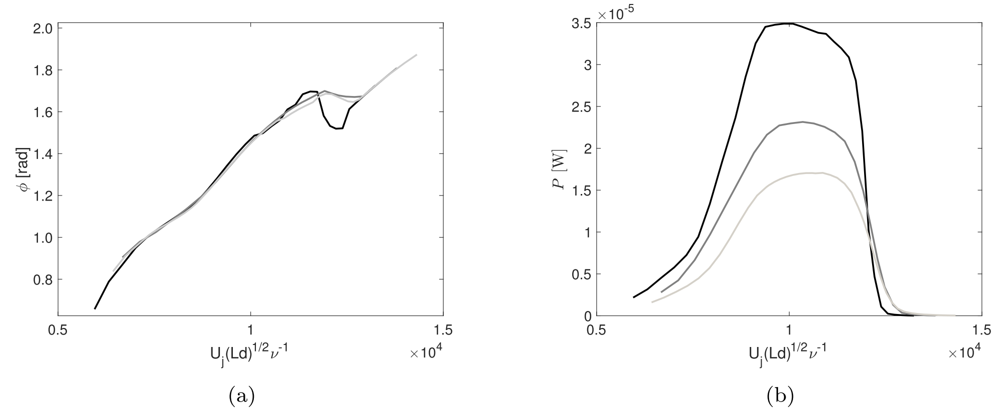

Fig. 17. Analytical results for Fig. 17a phase between Q_v and p_c and Fig. 17b average power $P = Q_v p_c$, as functions of the modified Reynolds number Re_m. Resonators A, B and C are indicated by colors black, gray and light gray, respectively.

The results indicate that the model is able to capture the Reynolds-number thresholds corresponding to the onset and cessation of self-sustained oscillations for all resonators examined in this study. In all cases, a consistent trend composed of three regimes is observed. First, at low Reynolds numbers, an increase of Re leads to a gradual rise in the cavity pressure p_c. As the Reynolds number is further increased, the second regime is achieved, where the cavity pressure remains approximately constant over a finite Reynolds-number range. The system enters the third regime when the Reynolds value crosses a critical limit, in which case p_c undergoes an abrupt decrease, indicating the cessation of self-sustained oscillations. This characteristic behavior can be interpreted using the analytical framework developed in the present model, as discussed in the following analysis.

First, a steady solution of Eq. (13) is obtained by assuming a harmonic forcing term of the form $\dot{q} = \hat{\dot{q}} e^{i\omega_v t}$, which yields

$$\hat{\Gamma} = \frac{\alpha U_j \hat{\dot{q}}}{i\omega_v + \frac{1}{\tau_d}}, \tag{16}$$

where $\hat{\Gamma}$ and $\hat{\dot{q}}$ are the complex representations of Γ and $\dot{q}$, respectively. The magnitude of $\hat{\Gamma}$ is given by

$$|\Gamma| = \frac{\alpha U_j |\dot{q}|}{\sqrt{\omega_v^2 + \left(\frac{1}{\tau_d}\right)^2}}. \tag{17}$$

At low Reynolds number, the vortex shedding frequency ω_v is moderate and the circulation decay time τ_d is reasonably large, allowing Eq. (17) to be approximated as

$$|\Gamma| \approx \frac{\alpha U_j |\dot{q}|}{\omega_v}. \tag{18}$$

Although ω_v is proportional to Re, its effect on the circulation amplitude $|\Gamma|$ remains moderate at low Reynolds values because U_j grows at a much higher rate than ω_v. This allows Γ to grow steadily with the Reynolds number. Since the volumetric flux Q_v injected into the cavity is proportional to Γ, the acoustic forcing p_c also increases progressively with Re, as shown in Fig. 16.

As the Reynolds number approaches a critical range, ω_v approximates to the acoustic eigenfrequency of the Helmholtz resonator in the absence of flow. In this regime, governed by Eq. (17), Q_v and p_c assume a phase difference of $\approx \pi/2$, as seen in Fig. 17a. This condition facilitates the sustained transfer of acoustic energy from the flow to the acoustic field, as illustrated in terms of averaged acoustic power $P = Q_v p_c$ in Fig. 17b. In fact, the maximum power is generated in the region where $\phi \approx \pi/2$ radians, corresponding to $Re_m \sim 1.1 \times 10^4$. This phase behavior agrees with the experimental data shown in the left columns of Figs. 10, 11, which correspond to the self-sustained oscillations of Resonators A, B and C at their maximum acoustic generation.

Further increases in flow velocity simultaneously enhance the vortex production term $\alpha U_j |\dot{q}|$ and the shedding frequency ω_v, while decreasing τ_d. These opposing trends balance one another, maintaining Γ on a nearly constant amplitude, resulting in an approximately constant cavity pressure.

Beyond a critical Reynolds number, the term $1/\tau_d$ increases much more rapidly than ω_v, implying that Eq. (17) can be approximated as

$$|\Gamma| \approx \alpha \tau_d U_j |\dot{q}|. \tag{19}$$

Because the circulation amplitude scales with a rapidly decreasing τ_d, the hydrodynamic forcing decreases, despite the increase in flow rate U_j. Simultaneously, detuning between the vortex shedding dynamics and the Helmholtz resonator eigenfrequency degrades the phase relationship required for efficient energy transfer. The combined effects lead to a sudden reduction in net acoustic power input, causing the self-sustained oscillation to collapse and the cavity pressure to drop abruptly.

6. Conclusions

The present study aimed at providing further insight into the feedback loop between acoustic and flow fields underlying whistling, with particular emphasis on systems characterized by long cavities and small orifices, represented by double-neck Helmholtz resonators subjected to a bias flow. The analysis focused on configurations within the parameter range $6.0 \leq L/d \geq 14$, which is typical of human whistling.

Initial analyses based on combined flow and acoustic measurements revealed new scaling relations in terms of Reynolds and Strouhal numbers. Within the self-sustained oscillation region, the sound pressure level measured with an external microphone scaled with the Strouhal number, exhibiting a consistent peak at $St \approx 0.32$ for all resonators. Furthermore, a collapse of the data from different geometries was achieved when the Strouhal number was plotted as a function of a modified Reynolds number given by $Re_m = U_j\sqrt{Ld}/\nu$. This result indicates that the interplay between viscous and inertial effects is governed not only by the local orifice diameter d, but also by the development of the flow along the cavity length L.

Experimental analyses based on two-point coherence and cross-power spectral density between particle velocity (obtained from PIV) and acoustic pressure indicated that the dominant acoustic generation occurs inside the resonator chamber rather than in the issuing jet, in contrast to assumptions commonly reported in previous literature. The measurements further show that the region of maximum acoustic production is located approximately $2.3d$ downstream of the upstream orifice.

PIV measurements revealed that vortices generated at the upstream orifice during self-sustained oscillations dissipate before reaching the downstream orifice. This observation is consistent with the findings of Wilson et al. [37], who reported that inserting metallic wool into similar resonators did not suppress oscillations, and supports the view that long-cavity whistles do not operate through the classical Rayleigh feedback mechanism originally proposed for hole tones.

In contrast to hole tones, pipe tones, ring tones, and Rossiter-type oscillations, where sound generation and feedback rely on the interaction of coherent vortices with a downstream edge or obstacle [23–29,31–33,58], the present results indicate that the dominant feedback mechanism is governed by localized hydrodynamic-acoustic coupling within the resonator cavity. These findings extend the conclusions of Wilson et al. [37] and complement the studies of Henrywood and Agarwal [25] and Vovk et al. [39], demonstrating that long-cavity Helmholtz whistles constitute a distinct class of self-sustained oscillator whose dynamics are controlled primarily by cavity-flow interaction rather than by downstream vortex impingement.

To investigate the onset and extinction of self-sustained oscillations, an empirical model was developed based on a two-degree-of-freedom lumped acoustic system coupled to a nonlinear van der Pol oscillator representing vortex shedding at the upstream neck. Acoustic dynamics were described in terms of neck volumetric flows and cavity pressure, while hydrodynamic effects were incorporated through a circulation variable that introduces a fluctuating volumetric injection into the cavity. The cavity pressure feeds back into the oscillator, forming a nonlinear hydrodynamic-acoustic loop, which was capable of reproducing the onset, saturation, lock-in, and collapse of oscillations, with good agreement between analytical predictions and experimental observations.

Although several model parameters were identified empirically, each retains a clear physical interpretation associated with vortex formation, convection, decay, and hydrodynamic-acoustic coupling. The calibrated values remain physically plausible and consistent with geometric and flow scaling. Importantly, a single parameter set reproduces multiple independent experimental features, including onset, saturation, lock-in, and abrupt extinction, demonstrating that the model captures the essential underlying physics.

Nevertheless, the proposed model is presently capable of capturing only the self-sustained oscillation mechanism observed in Helmholtz resonators with long cavities, i.e., for configurations satisfying $L/d > 3$. In addition, variations in the d/t ratio or in the orifice geometry, for example, sharp-edged orifices instead of the smooth circular geometry considered in the present manuscript, are expected to modify the end-correction parameter, a. Therefore, for the model to accurately predict self-sustained oscillations in configurations with different orifice geometries, the corresponding end correction must first be determined independently.

Analyses based on the model and experimental data suggested that self-sustained oscillations arise from the coupling between vortex shedding at the upstream neck and the acoustic response of the cavity-neck system. The bias flow generates shear-layer instabilities that produce vortices, which inject unsteady flow into the cavity and excite Helmholtz-type pressure oscillations. In turn, the resulting cavity pressure modulates the jet dynamics and subsequent vortex formation, establishing a closed hydrodynamic-acoustic feedback loop. When the shedding frequency approaches the acoustic eigenfrequency and the phase between injected flow and cavity pressure is favorable, energy is transferred from the mean flow to the acoustic field, sustaining oscillations. Otherwise, detuning and losses weaken the coupling and the oscillations decay.

Future work should extend the present model to include predictions of far-field sound radiation and the influence of the difference between downstream and upstream orifice diameters.

CRediT authorship contribution statement

Andrey R. da Silva: Writing – original draft, Validation, Supervision, Methodology, Investigation, Funding acquisition, Formal analysis, Data curation, Conceptualization; **Niklaus Lima:** Visualization, Validation, Methodology, Investigation, Formal analysis, Data curation; **Julio Cordioli:** Writing – original draft, Validation, Software, Investigation, Funding acquisition, Formal analysis; **Tsukasa Yoshinaga:** Writing – original draft, Visualization, Methodology, Investigation, Formal analysis, Conceptualization; **Tercio L. Pereira:** Writing – original draft, Visualization, Methodology, Investigation, Formal analysis.

Data availability

Data will be made available on request.

Declaration of competing interest

The authors declare that they have not identified any competing financial interests or personal relationships that could have appeared to influence the work reported in this paper.

Acknowledgment

The first author thanks CNPq for grant N.402741/2023-4. J.C. aknowledges CNPq grant N.315000/2021-0. The authors would like to thank the reviewers for the substantial improvements on the original manuscript and R. Resener for helping with FEM simulations.

References

[1] G. Nakiboglu, Aeroacoustics of corrugated pipes, 2012,
[2] G. Nakiboglu, S.P.C. Belfroid, J. Golliard, A. Hirschberg, On the whistling of corrugated pipes: effect of pipe length and flow profile, J. Fluid Mech. 672 (2011) 78–108.
[3] O.M. Umurhan, Exploration of fundamental matters of acoustic instabilities in combustion chambers, 2000. https://api.semanticscholar.org/CorpusID:1495868.
[4] G.J. Bloxsidge, A.P. Dowling, P.J. Langhorne, Reheat buzz: an acoustically coupled combustion instability. Part 2. Theory, J. Fluid Mech. 193 (1988) 445–473.
[5] T. KUDO, Y. KOMATSU, K. MAEDA, M. NISHIMURA, Techniques for reducing low-frequency fluctuations in aeroacoustic wind tunnels, J. Environ. Eng. 4 (2) (2009) 289–301.
[6] L. Jin, X.B. Deng, X. Wang, J. Zhang, W. Zeng, Review of mechanisms and suppression methods for low-frequency pressure fluctuations in open-jet wind tunnels, Appl. Sci. 13 (19) (2023) 10808.
[7] Q. Wang, X. Chen, Y. Zhang, An overview of automotive wind noise and buffeting active control, SAE Int. J. Veh. Dyn. Stab. NVH 05 (4) (2021) 443–458.
[8] S. Cao, Z. Zhang, Q. Zhang, Z. Xu, W. Lin, Energy transfer characteristics of sunroof wind buffeting noise via dynamic mode decomposition, J. Sound Vib. 555 (2023) 117724. https://doi.org/10.1016/j.jsv.2023.117724
[9] F.L. Eisinger, J.T. Francis, Acoustically induced structural fatigue of piping systems, J. Press. Vessel Technol. 121 (4) (1999) 438–443.
[10] F.L. Eisinger, R.E. Sullivan, Vibration fatigue of centrifugal fan impeller due to structural-acoustic coupling and its prevention: a case study, in: Volume 9: 6th FSI, AE and FIV and N Symposium, PVP2006-ICPVT-11, ASMEDC, 2006, p. 47–53.
[11] M. Belyk, B.G. Schultz, J. Correia, D.S. Beal, S.A. Kotz, Whistling shares a common tongue with speech: bioacoustics from real-time MRI of the human vocal tract, Proc. R. Soc. B Biol. Sci. 286 (1911) (2019) 20191116.
[12] A. Rialland, Phonological and phonetic aspects of whistled languages, Phonology 22 (2) (2005) 237–271.
[13] C. Sondhauss, Ueber die beim Ausstromen der luft entstehenden tone, Ann. Phys. 167 (1) (1854) 126–147.
[14] L.R. John William Strutt, The Theory of Sound, Volume II, Macmillan and Co., London, 1st edition, London, 1878. Available in later reprints and online archives.
[15] R.C. Chanaud, Aerodynamic whistles, Sci. Am. 222 (1) (1970) 40–47.
[16] O.M. Phillips, The intnesity of Aeolian tones, J. Fluid Mech. 1 (6) (1956) 607–624.
[17] R.T. Keefe, Investigation of the fluctuating forces acting on a stationary circular cylinder in a subsonic stream and of the associated sound field, J. Acoust. Soc. Am. 34 (11) (1962) 1711-1714.
[18] R. SCHLINKER, R. AMIET, Vortex noise from nonrotating cylinders and airfoils, in: 14th Aerospace Sciences Meeting, American Institute of Aeronautics and Astronautics, 1976.
[19] H. Fujita, The characteristics of the Aeolian tone radiated from two-dimensional cylinders, Fluid Dyn. Res. 42 (1) (2010) 015002.
[20] W.E. Benton, On edge-tones (I), Proc. Phys. Soc. Lond. 38 (1) (1925) 109–126.
[21] J.W. Coltman, Jet drive mechanisms in edge tones and organ pipes, J. Acoust. Soc. Am. 60 (3) (1976) 725–733.
[22] I. Vaik, R. Varga, G. Paal, Frequency and phase characteristics of the edge tone, Part II, Period. Polytech. Mech. Eng. 58 (1) (2014) 69–76.
[23] M.A. Langthjem, M. Nakano, A numerical simulation of the hole-tone feedback cycle based on an axisymmetric discrete vortex method and Curle's equation, J. Sound Vib. 288 (1-2) (2005) 133–176. https://doi.org/10.1016/j.jsv.2004.12.023
[24] A. Meganathan, A. Vakili, An experimental study of acoustic and flow characteristics of hole tones, in: 44th AIAA Aerospace Sciences Meeting and Exhibit, American Institute of Aeronautics and Astronautics, 2006. https://doi.org/10.2514/6.2006-1015
[25] R.H. Henrywood, A. Agarwal, The aeroacoustics of a steam kettle, Phys. Fluids 25 (10) (2013) 107101.
[26] R. Longobardi, D. Fabre, P. Bonnefis, V. Citro, F. Giannetti, P. Luchini, Studying Sound Production in the Hole-Tone Configuration Using Compressible and Incompressible Global Stability Analyses, Springer International Publishing, 2021, p. 251–263. https://doi.org/10.1007/978-3-030-55594-8_23
[27] R.C. Chanaud, A. Powell, Some experiments concerning the hole and ring tone, J. Acoust. Soc. Am. 37 (5) (1965) 902–911.
[28] K. Matsuura, K. Mukai, M.A. Langthjem, Computational and experimental study on the mechanism of ring tone, Int. J. Comput. Methods Exp. Meas. 11 (1) (2023) 9–16.
[29] A.B.C. Anderson, A circular-orifice number describing dependency of primary pfeifenton frequency on differential pressure, gas density, and orifice geometry, J. Acoust. Soc. Am. 25 (4) (1953) 626–631.
[30] D. Rockwell, E. Naudascher, Review: self-sustaining oscillations of flow past cavities, J. Fluids Eng. 100 (2) (1978) 152–165.
[31] C.K.W. Tam, P.J.W. Block, On the tones and pressure oscillations induced by flow over rectangular cavities, J. Fluid Mech. 89 (2) (1978) 373–399.
[32] J. Malone, M. Debiasi, J. Little, M. Samimy, Analysis of the spectral relationships of cavity tones in subsonic resonant cavity flows, Phys. Fluids 21 (5) (2009) 1–9.
[33] J.W. Coltman, Sounding mechanism of the flute and organ pipe, J. Acoust. Soc. Am. 44 (4) (1968) 983–992.
[34] N.H. Fletcher, Nonlinear interactions in organ flue pipes, J. Acoust. Soc. Am. 56 (2) (1974) 645–652.
[35] M.S. Howe, Contributions to the theory of aerodynamic sound, with application to excess jet noise and the theory of the flute, J. Fluid Mech. 71 (4) (1975) 625–673.
[36] M.P. Verge, B. Fabre, W.E.A. Mahu, A. Hirschberg, R.R. van Hassel, A.P.J. Wijnands, J.J. de Vries, C.J. Hogendoorn, Jet formation and jet velocity fluctuations in a flue organ pipe, J. Acoust. Soc. Am. 95 (2) (1994) 1119–1132.
[37] T.A. Wilson, G.S. Beavers, M.A. DeCoster, D.K. Holger, M.D. Regenfuss, Experiments on the fluid mechanics of whistling, J. Acoust. Soc. Am. 50 (1B) (1971) 366–372.
[38] A. Azola, J. Palmer, R. Mulheren, R. Hofer, F. Fischmeister, W.T. Fitch, The physiology of oral whistling: a combined radiographic and MRI analysis, J. Appl. Physiol. 124 (1) (2018) 34–39.
[39] I.V. Vovk, V.T. Matsypura, Y.P. Trotsenko, Excitation of self-sustained oscillations by a flow of liquid in a cylindrical duct with two diaphragms, J. Math. Sci. 247 (2) (2020) 258–275.

[40] M. Mori, S. Fukuda, Frequency response of the vocal tract considering the glottis opening area during human whistling, Electron. Commun. Jpn. 103 (8) (2020) 3–8.
[41] M. Mori, T. Washida, M. Kawarada, M. Okamoto, Reconsideration of the principle of sound resonance in human whistling using the vocal tract model, in: 2023 3rd International Conference on Electrical, Computer, Communications and Mechatronics Engineering (ICECCME), IEEE, Tenerife, Canary Islands, Spain, 2023, pp. 1–5.
[42] W. Thielicke, R. Sonntag, Particle image velocimetry for MATLAB: accuracy and enhanced algorithms in PIVlab, J. Open Res. Softw. 9 (1) (2021) 12. https://doi.org/10.5334/jors.334
[43] A. Selamet, Z.L. Ji, R.A. Kach, Wave reflections from duct terminations, J. Acoust. Soc. Am. 109 (4) (2001) 1304–1311.
[44] A.R.D. Silva, P.H. Mareze, A. Lenzi, Approximate expressions for the reflection coefficient of ducts terminated by circular flanges, J. Braz. Soc. Mech. Sci. Eng. 34 (2) (2012) 219–224.
[45] N.M. Papadakis, G.E. Stavroulakis, Tunable Helmholtz resonators using multiple necks, Micromachines 14 (10) (2023) 1932.
[46] M.A. Langthjem, M. Nakano, A numerical study of the hole-tone phenomenon subjected to non-axisymmetric shape perturbations of the jet nozzle, Theor. Comput. Fluid Dyn. 29 (3) (2015) 127–153.
[47] J.E. Rossiter, Wind-Tunnel Experiments on the Flow Over Rectangular Cavities at Subsonic and Transonic Speeds, Reports and Memoranda No. 3438, Aeronautical Research Council, Royal Aircraft Establishment, 1964.
[48] J.C. DEL ÁLAMO, J. JIMÉNEZ, Estimation of turbulent convection velocities and corrections to Taylor's approximation, J. Fluid Mech. 640 (2009) 5–26.
[49] B.R. Noack, F. Ohle, H. Eckelmann, On cell formation in vortex streets, J. Fluid Mech. 227 (1991) 293–308.
[50] S. Balasubramanian, R.A. Skop, A nonlinear oscillator model for vortex shedding from cylinders and cones in uniform and shear flows, J. Fluids Struct. 10 (3) (1996) 197–214.
[51] R. Hollenbach, R. Kielb, K. Hall, A fluid-structure interaction tool using a van der pol-based reduced-order model for buffet and nonsynchronous vibrations, J. Turbomach. 145 (1) (2022) 1–11.
[52] B. Phillips, Effects of High-Wave Amplitude and Mean Flow on a Helmholtz Resonator, NASA Technical Memorandum NASA TM X-1582, NASA Lewis Research Center, 1968. https://ntrs.nasa.gov/api/citations/19680013954/downloads/19680013954.pdf.
[53] A.I. Komkin, M.A. Mironov, S.I. Yudin, On the attached length of orifices, Acoust. Phys. 58 (6) (2012) 628–632. https://doi.org/10.1134/S1063771012050090
[54] M.C.A.M. Peters, A. Hirschberg, A.J. Reijnen, A.P.J. Wijnands, Damping and reflection coefficient measurements for an open pipe at low mach and low Helmholtz numbers, J. Fluid Mech. 256 (1993) 499–534. https://doi.org/10.1017/s0022112093002861
[55] A.R. da Silva, G.P. Scavone, A. Lefebvre, Sound reflection at the open end of axisymmetric ducts issuing a subsonic mean flow: a numerical study, J. Sound Vib. 327 (3–5) (2009) 507–528. https://doi.org/10.1016/j.jsv.2009.06.027
[56] R.P. Benedict, J.S. Wyler, G.B. Brandt, The effect of edge sharpness on the discharge coefficient of an orifice, J. Eng. Power 97 (4) (1975) 576–581.
[57] M.S. Howe, Sound produced by a vortex ring interacting with an aperture of variable radius, Int. J. Aeroacoustics 7 (2) (2008) 103–122.
[58] D. Rockwell, E. Naudascher, Review:self-sustaining oscillations of flow past cavities, J. Fluids Eng. 100 (2) (1978) 152–165.